

# Chapter 3

---

### **3. BARE ZINC OXIDE (ZnO) AND TIN DIOXIDE (SnO<sub>2</sub>) NANOCATALYSTS FOR REGIOSELECTIVE FRIEDEL-CRAFTS ACYLATION REACTION**

This chapter of the thesis is divided into three sections describing the complete characterization of bare ZnO and SnO<sub>2</sub> nanocatalysts synthesized via hydro/solvothermal method. The activity of the bare metal oxide nanocatalysts have been tested for the regioselective Friedel-Crafts acylation reaction.

#### **3.1 Prologue**

The Friedel-Crafts (FC) acylation of aromatic substrates with acid halides is a fundamental and important conversion in organic synthesis [1–3]. In particular, regioselective FC acylation has great potential in chemical industry for the synthesis of aromatic ketones that are involved in preparation of various synthetic intermediates, [4] chemical feedstocks, [5] pharmaceuticals [6] and fine chemicals [7]. Although the aromatic ketones have tremendous applications, yet conventional strategies to synthesize such ketones usually suffer from major challenges of complicated synthetic procedures and environmental concerns [8, 9]. The use of homogeneous catalysts e.g. protic acids, [10] soluble metal halides, [11] substituted anhydrides [12] in stoichiometric amount and other homogeneous catalysts e.g. Ln(OTf)<sub>3</sub>-LiClO<sub>4</sub>, [13] LiClO<sub>4</sub>-acyl anhydride complex, [14] (PhCN)<sub>2</sub>PtCl<sub>2</sub>/AgSbF<sub>6</sub>, [15] Re-Br(CO)<sub>5</sub> [16] and so on in catalytic amount spectacle certain progress in the reaction. However, the industrial application of these homogeneous catalysts is also associated with various shortcomings due to the non-economical reaction process and environmental issues [16, 17]. Therefore, development of a highly reactive and economical catalyst system with less environmental disputes is quiet challenging. As a result, efforts have been directed to the synthesis of solid acid catalysts that exhibit high activity and selectivity and are easily recoverable [18]. So far, several solid acid catalysts have been used including sulfated ZrO<sub>2</sub> or Fe<sub>2</sub>O<sub>3</sub>, [19, 20] sulfated Al<sub>2</sub>O<sub>3</sub>-ZrO<sub>2</sub> (or TiO<sub>2</sub>), [21, 22] acidic zeolite, [23] clays, [24] metal oxides, [25] heteropolyacid salts, [26] Nafion [27] etc. Metal oxides, in particular, have large number of edge and corner sites responsible for adsorbing and activating reactant molecules and are readily available, and non-corrosive in nature [28]. Researchers are currently focused on the synthesis and application of metal or metal oxide nanocatalysts for diverse organic transformations because catalysts in the

nanometric regime offer better reactivity and selectivity [29, 30]. However, the application of metal oxide nanocatalysts in regioselective FC acylation is very scarce in previous reports. Hence, different ZnO and SnO<sub>2</sub> nanocatalysts have been synthesized, characterized and employed for the FC acylation of aromatic compounds. The details about the properties of ZnO and SnO<sub>2</sub> are briefly described in the Chapter 1.

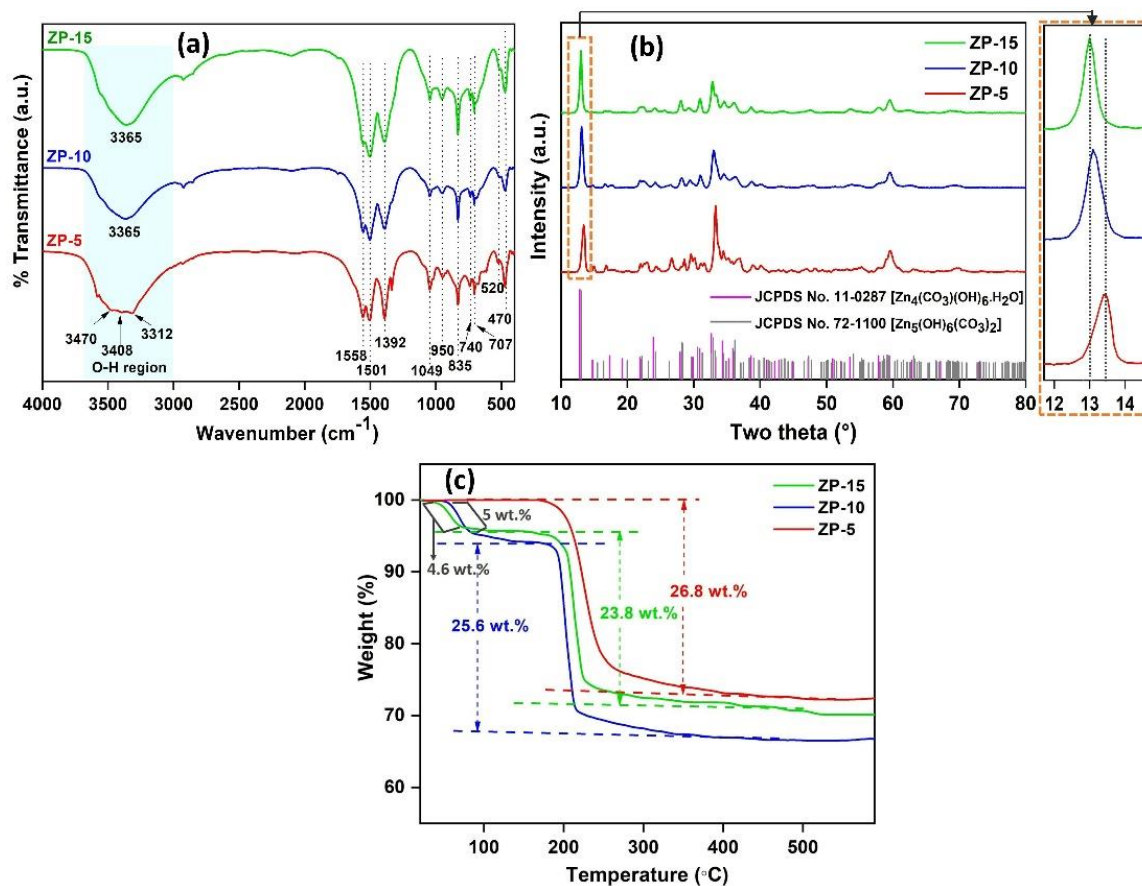
### **Section 3A: Time-driven morphology evolution and catalytic activity of porous ZnO hierarchical nanostructures**

In this section, we have discussed the complete characterization of ZnO hierarchical nanostructures (HNs) synthesized via a template-free precursor mediated hydrothermal route by varying the hydrothermal reaction time (5, 10, and 15 h) with subsequent calcination at 400 °C for 4 h. The catalytic activity of the synthesized HNs towards Friedel-Crafts acylation reaction has been discussed herein. The procedures for synthesis of ZnO HNs, characterization techniques and catalytic reaction are described in Chapter 2.

#### **3A.1 Results and discussion**

##### ***3A.1.1 Characterization of the ZnO hierarchical nanostructures***

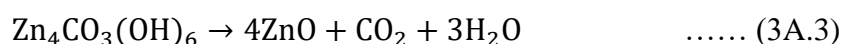
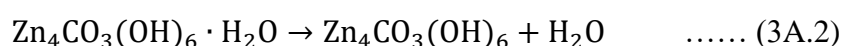
The ZnO precursors are first characterized by using FTIR and the obtained spectra are shown in Figure 3A.1a. All the spectra are similar to one other with the presence of characteristic bands in the range 707-1501 cm<sup>-1</sup> which are attributable to  $\nu_1$  symmetric CO<sub>3</sub><sup>2-</sup> stretching (1049 cm<sup>-1</sup>),  $\nu_2$  out-of-plane OCO bending (835 cm<sup>-1</sup>),  $\nu_3$  asymmetric CO<sub>3</sub><sup>2-</sup> stretching (1501, 1392 cm<sup>-1</sup>), and  $\nu_4$  asymmetric OCO bending (707, 740 cm<sup>-1</sup>) modes [31–33]. The presence of “Zn–OH” bonding and –COO<sup>-</sup> groups are also observed at 948 cm<sup>-1</sup> and 1558 cm<sup>-1</sup>, respectively [34, 35]. The bands (520 cm<sup>-1</sup> and 470 cm<sup>-1</sup>) at the lower mid-infrared region are ascribable to the Zn–O vibrations in the samples [35]. However, the broad band in the O-H region for ZP-5 splits into three peaks (3470, 3408 and 3312 cm<sup>-1</sup>), whereas ZP-10 and ZP-15 show a single symmetrical broad peak (3365 cm<sup>-1</sup>) in this region. To further analyze this difference, powder XRD analysis is carried out for the ZnO precursors and the diffractograms are presented in Figure 3A.1b.



**Figure 3A.1** XRD patterns (a), FTIR spectra (b) and TGA curves (c) of the synthesized ZnO precursors.

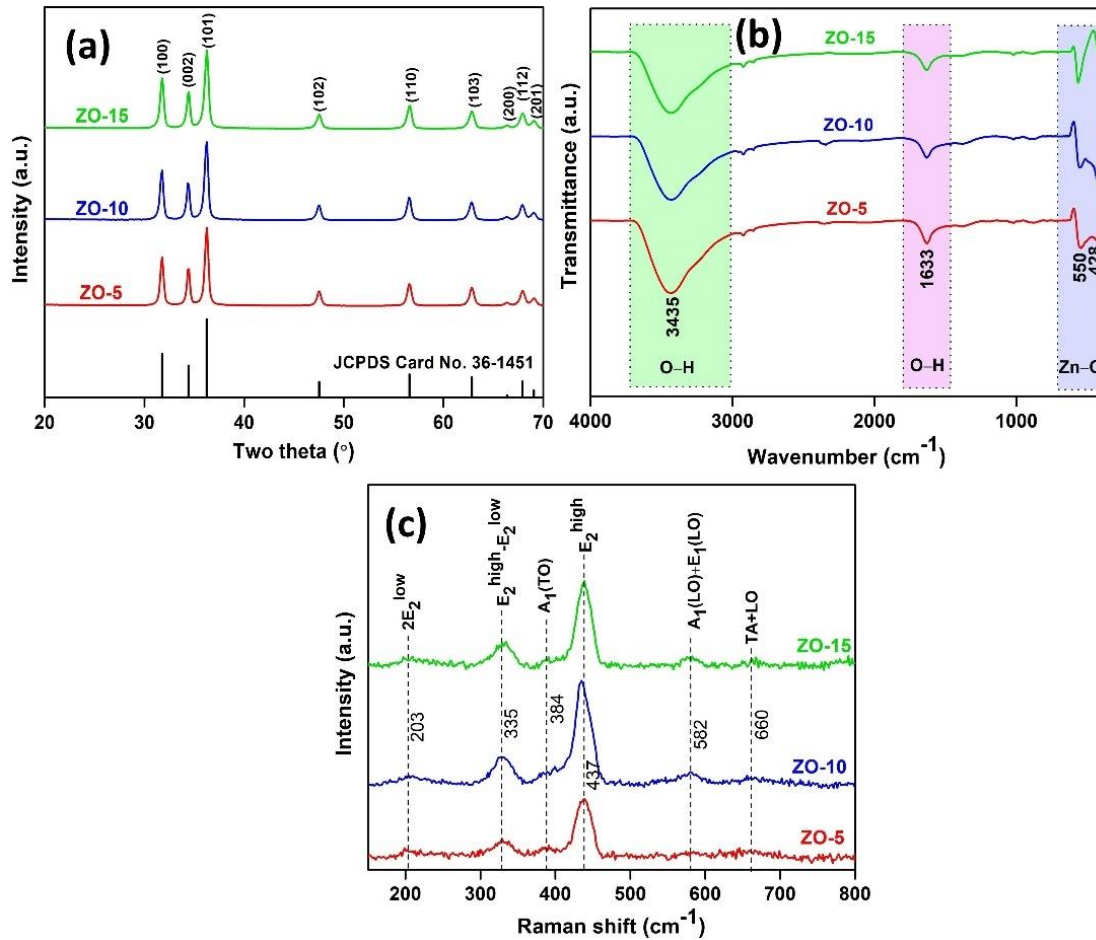
XRD analysis reveals that the diffraction peaks of all the precursors correspond to mixed phases of zinc carbonate hydroxide or hydrozincite [Zn<sub>5</sub>(CO<sub>3</sub>)<sub>2</sub>(OH)<sub>6</sub>] (JCPDS 072-1100) and zinc carbonate hydroxide hydrate [Zn<sub>4</sub>CO<sub>3</sub>(OH)<sub>6</sub>·H<sub>2</sub>O] (JCPDS 011-0287) [36, 37]. As the hydrothermal reaction time increases, the diffraction peaks corresponding to zinc carbonate hydroxide hydrate become more pronounced as evidenced by the peak shifting (magnified image in Figure 3A.1b) towards zinc carbonate hydroxide hydrate phase for precursors ZP-10 and ZP-15. This observation corroborates well with the FTIR results. As the primary phase of precursors ZP-10 and ZP-15 is zinc carbonate hydroxide hydrate, the FTIR spectra for these precursors show single O-H band corresponding to the presence of -OH groups of non-structural adsorbed H<sub>2</sub>O molecules of the hydrated basic zinc carbonate [32]. On the other hand, the three peaks in the O-H region of the FTIR spectrum for ZP-5 can be ascribed to the structural -OH groups in hydrozincite that show three different types of interactions corresponding to the different hydrogen bond acceptor strengths of carbonate oxygen atoms [31]. To

examine the conversion process of the ZnO precursors during calcination, TGA analysis is carried out and the corresponding TGA curves are presented in Figure 3A.1c. The TGA curve of ZP-5 depicts a single weight loss step in the temperature range 180–350 °C that can be attributed to the release of CO<sub>2</sub> and H<sub>2</sub>O from the thermal decomposition of the Zn<sub>5</sub>(CO<sub>3</sub>)<sub>2</sub>(OH)<sub>6</sub> primary phase of the precursor. The TGA curves of ZP-10 and ZP-15 display two weight loss steps. The first weight loss in the temperature range 50–100 °C could be due to the elimination and vaporization of water of crystallization and adsorbed water molecules from the Zn<sub>4</sub>CO<sub>3</sub>(OH)<sub>6</sub>·H<sub>2</sub>O precursor. The second weight loss step can be attributed to the thermal decomposition of Zn<sub>4</sub>CO<sub>3</sub>(OH)<sub>6</sub> with the release of CO<sub>2</sub> and H<sub>2</sub>O. The following reactions (equations 3A.1–3A.3) illustrate the decomposition process of Zn<sub>5</sub>(CO<sub>3</sub>)<sub>2</sub>(OH)<sub>6</sub>, Zn<sub>4</sub>CO<sub>3</sub>(OH)<sub>6</sub>·H<sub>2</sub>O and Zn<sub>4</sub>CO<sub>3</sub>(OH)<sub>6</sub> with theoretical weight loss percentages of ~26 %, 4 % and 23 %, respectively [11,12].



As expected, the calculated weight loss percentages from Figure 3A.1c are comparable to the theoretically calculated values. The slight variations in the values of weight loss percentages may be accomplished to the presence of mixed phases in the samples.

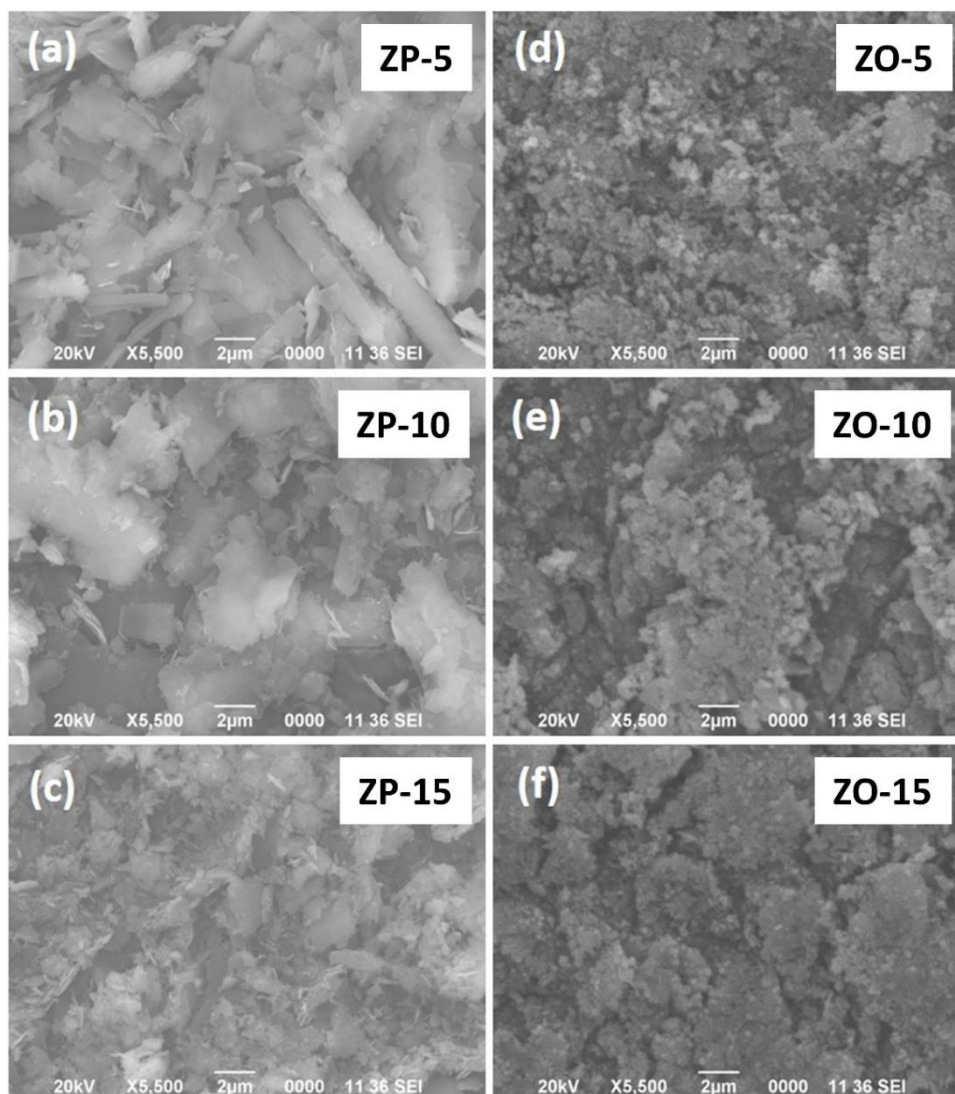
Figure 3A.2a displays the XRD patterns of the calcined samples. All the diffraction peaks are indexed to (100), (002), (101), (102), (110), (103), (200), (112), and (201) planes of hexagonal wurtzite structure of ZnO (JCPDS 36-1451) [38]. No secondary phase is observed in the synthesized ZnO, revealing the high purity of the samples. The sharp peaks show that the ZnO samples are well crystallized. By applying the Debye–Scherrer equation (mentioned in Chapter 2) to the diffraction peaks, the average crystallite sizes of ZO-5, ZO-10 and ZO-15 are estimated to be 20, 19 and 18 nm, respectively. The FTIR spectroscopic analysis of the ZnO samples (Figure 3A.2b) shows absorption bands at 3435 and 1633 cm<sup>-1</sup> attributed to vibrations of free H<sub>2</sub>O molecules and –OH groups adsorbed onto the surface of the oxides [39]. The absorption bands at 550 and 428 cm<sup>-1</sup> are assigned to the stretching vibration of Zn–O bond [40, 41].



**Figure 3A.2** XRD patterns (a), FTIR spectra (b) and Raman spectra (c) of the synthesized ZnO samples.

The micro-Raman analyses of the ZnO samples are conducted at room temperature and the results are presented in Figure 3A.2c. Wurtzite ZnO belongs to  $C_{6v}^4$  ( $P6_3mc$ ) space group in which the optical phonon modes are given by  $\Gamma_{\text{opt}} = A_1 + 2B_1 + E_1 + 2E_2$ , where  $B_1$  modes are silent and  $A_1$ ,  $E_1$  and  $E_2$  are Raman active modes [42]. Among them,  $A_1$  and  $E_1$  modes are polar and divided into two components: transverse optical ( $A_1(\text{TO})$  and  $E_1(\text{TO})$ ) and longitudinal optical ( $A_1(\text{LO})$  and  $E_1(\text{LO})$ ). On the other hand,  $E_2$  mode is composed of two phonon modes: low frequency ( $E_2^{\text{low}}$ ) and high frequency ( $E_2^{\text{high}}$ ), corresponding to vibrations of the heavy Zn sublattice and oxygen atoms, respectively [43]. The Raman spectra of the synthesized samples exhibit basic phonon modes centered at 203, 384, 437 and 582  $\text{cm}^{-1}$  which correspond to  $2E_2^{\text{low}}$ ,  $A_1(\text{TO})$ ,  $E_2^{\text{high}}$  and  $A_1(\text{TO}) + E_1(\text{TO})$ , respectively [44, 45]. The multi phonon scattering modes centered at 335, 582 and 660  $\text{cm}^{-1}$  are ascribable to  $(E_2^{\text{high}} - E_2^{\text{low}})$ ,  $(A_1(\text{TO}) +$

$E_1(\text{TO})$ ) and (transverse acoustic (TA) + LO modes), respectively [45, 46]. The ZO-10 and ZO-15 exhibit more pronounced bands in the Raman spectra which implies that these samples are better crystallized compared to that of ZO-5.

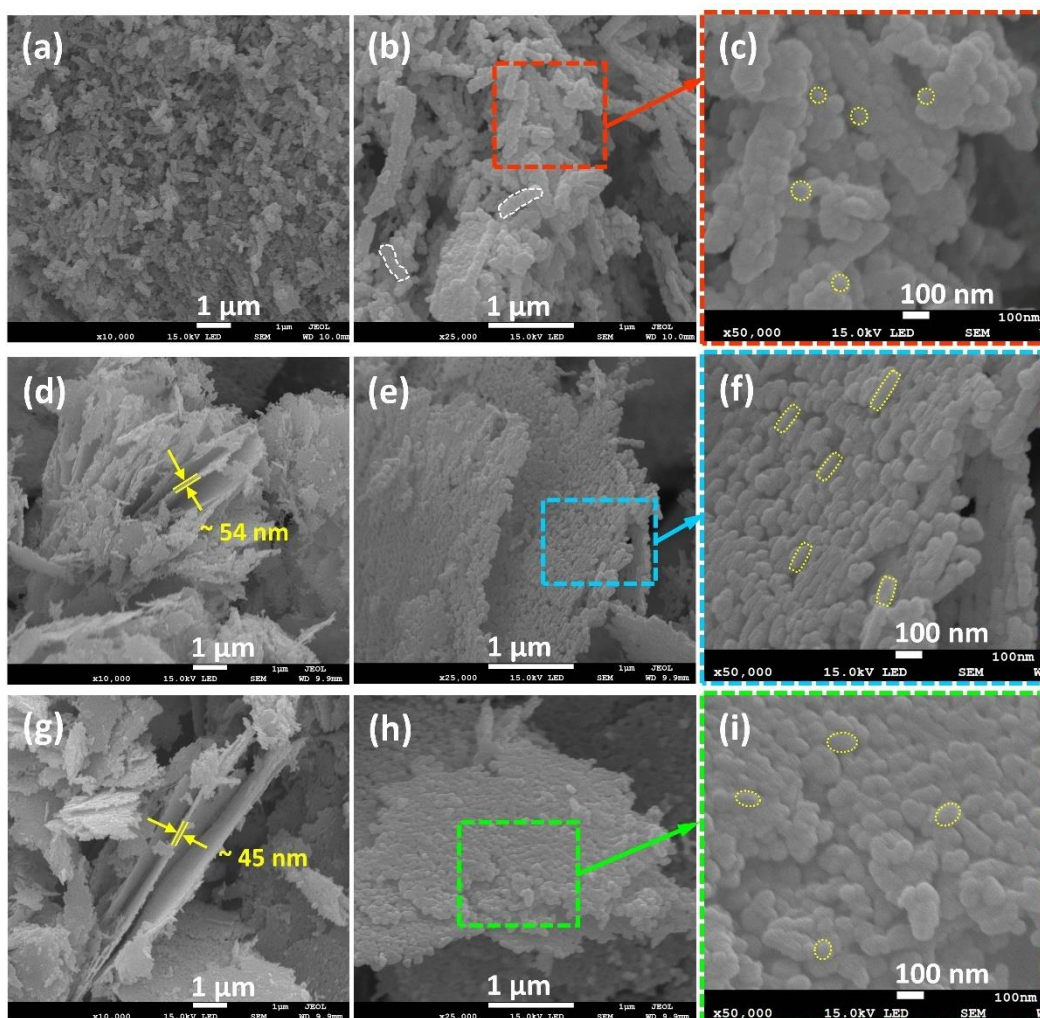


**Figure 3A.3** SEM micrographs of ZnO precursors (a-c) and ZnO samples (d-f).

Figure 3A.3 shows the SEM images of the as-synthesized ZnO before and after calcination. SEM image of the precursor ZP-5 demonstrates that several nanoflakes are stacked together giving a rod-like morphology (Figure 3A.3a). As the hydrothermal time increases, this morphology is gradually lost. The SEM images of ZP-10 and ZP-15 precursors show that both these precursors are composed of two dimensional nanoflakes distributed randomly across the whole sample (Figure 3A.3(b, c)). Upon calcination, all the ZnO precursors are transformed to agglomerated nanoparticles (Figure 3A.3d-f).



FESEM images of the calcined products ZO-5, ZO-10 and ZO-15 are also obtained as displayed in Figure 3A.4. The FESEM image of ZO-5 shows the presence of porous rod-

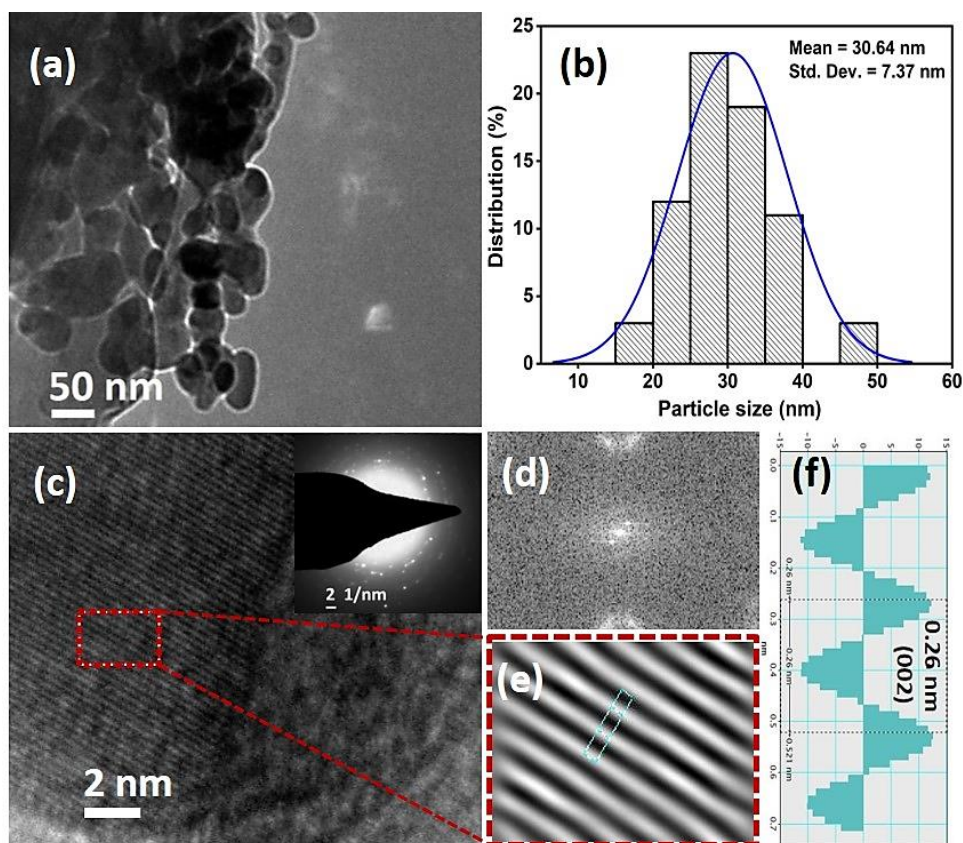


**Figure 3A.4** FESEM images of ZO-5 (a-c), ZO-10 (d-f) and ZO-15 (g-i) at different resolutions.

like hierarchical nanostructures (HNs) composed of nanoparticles (Figure 3A.4a–c). The pores are generated in the nanoarchitectures due to the release of  $\text{CO}_2$  and  $\text{H}_2\text{O}$  upon calcination [31]. On the other hand, FESEM images of the samples ZO-10 and ZO-15 display HNs comprising several porous random nanoflakes that have a thickness of  $\sim 54$  nm and  $\sim 45$  nm, respectively (Figure 3A.4d–i). It can be observed that the individual nanoflakes are composed of numerous elongated inter-connected nanoparticles with a diameter of  $\sim 30$ – $40$  nm. All these observations imply that the hydrothermal reaction time is a decisive factor for controlling morphology of the synthesized precursors and thereby alters the morphology of the resultant ZnO samples.



Figure 3A.5 displays the TEM analysis for ZO-10 sample. The TEM image in Figure 3A.5a shows the presence of nanoparticles with elongated shape and irregular sizes. The particle size distribution of ZO-10 shows that the sample has an average



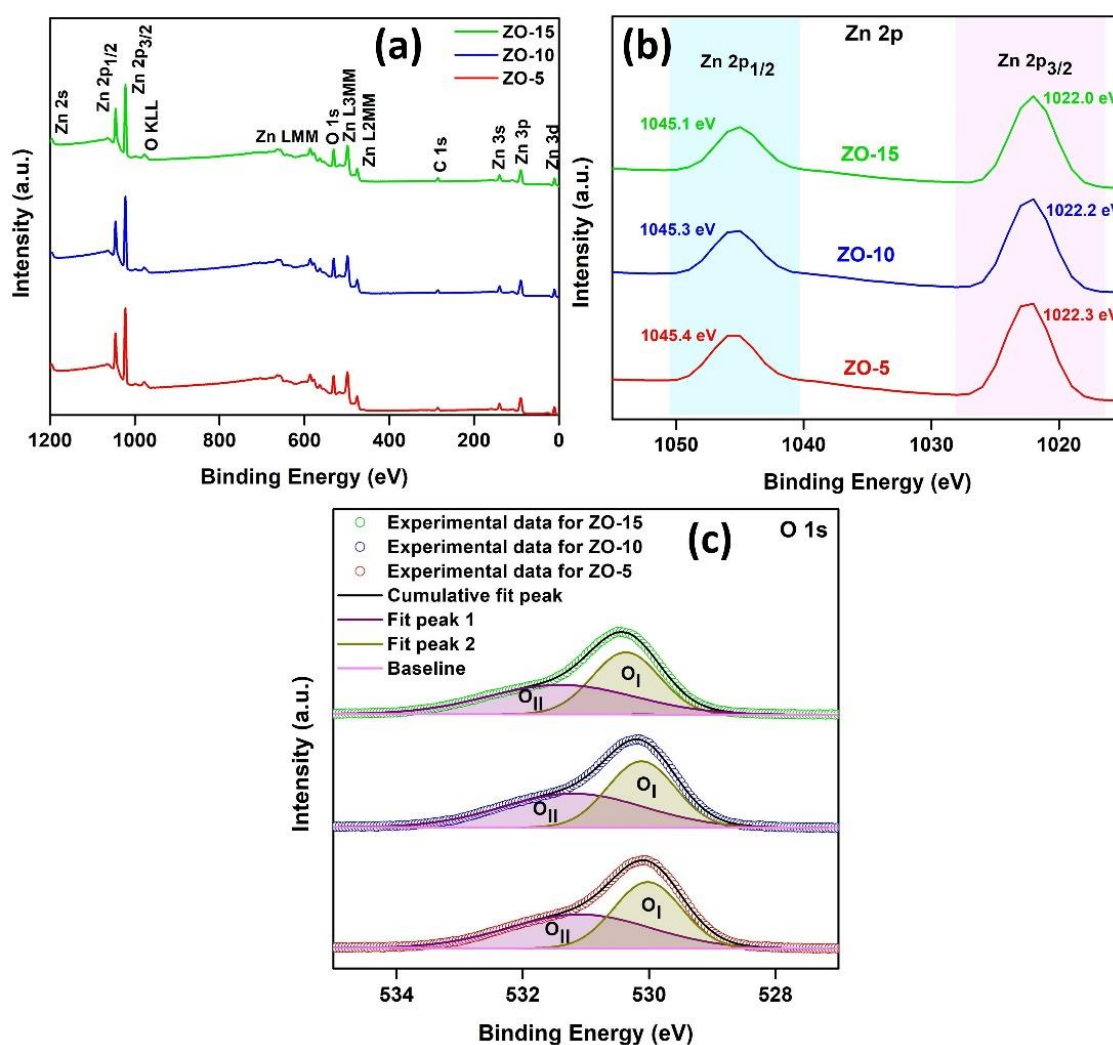
**Figure 3A.5** TEM image (a), particle size distribution (b), HRTEM image (c), fast Fourier transform (FFT) image (d), inverse FFT (IFFT) image (e) and the live profile of IFFT (f) of the ZO-10 sample.

particle diameter of 30.64 nm (Figure 3A.5b). The clearly visible lattice fringes indicate that the nanoparticles are highly crystalline in nature (Figure 3A.5c). The lattice fringes of ZO-10 with a d-spacing of 0.26 nm corresponds to (002) plane of wurtzite ZnO as observed from live profile of IFFT image (Figure 3A.5f). The TEM images and their corresponding particle size distributions for ZO-5 and ZO-15 are displayed in Figure A.1 of Appendix. The average particle diameters of the ZnO samples are summarized in Table 3A.1. The results imply that the particle sizes of the synthesized ZnO samples do not follow any trend with increasing hydrothermal reaction time unlike the morphology.

**Table 3A.1** Average particle diameters of the ZnO samples.

Entry	Sample	Average particle diameter (nm)
1	ZO-5	34.01
2	ZO-10	30.64
3	ZO-15	39.70

XPS analysis is conducted to analyze the chemical state and composition of the ZnO nanostructures and the spectra are presented in Figure 3A.6. The survey spectra of the samples in Figure 3A.6a indicate the presence of Zn and O as the major elements.

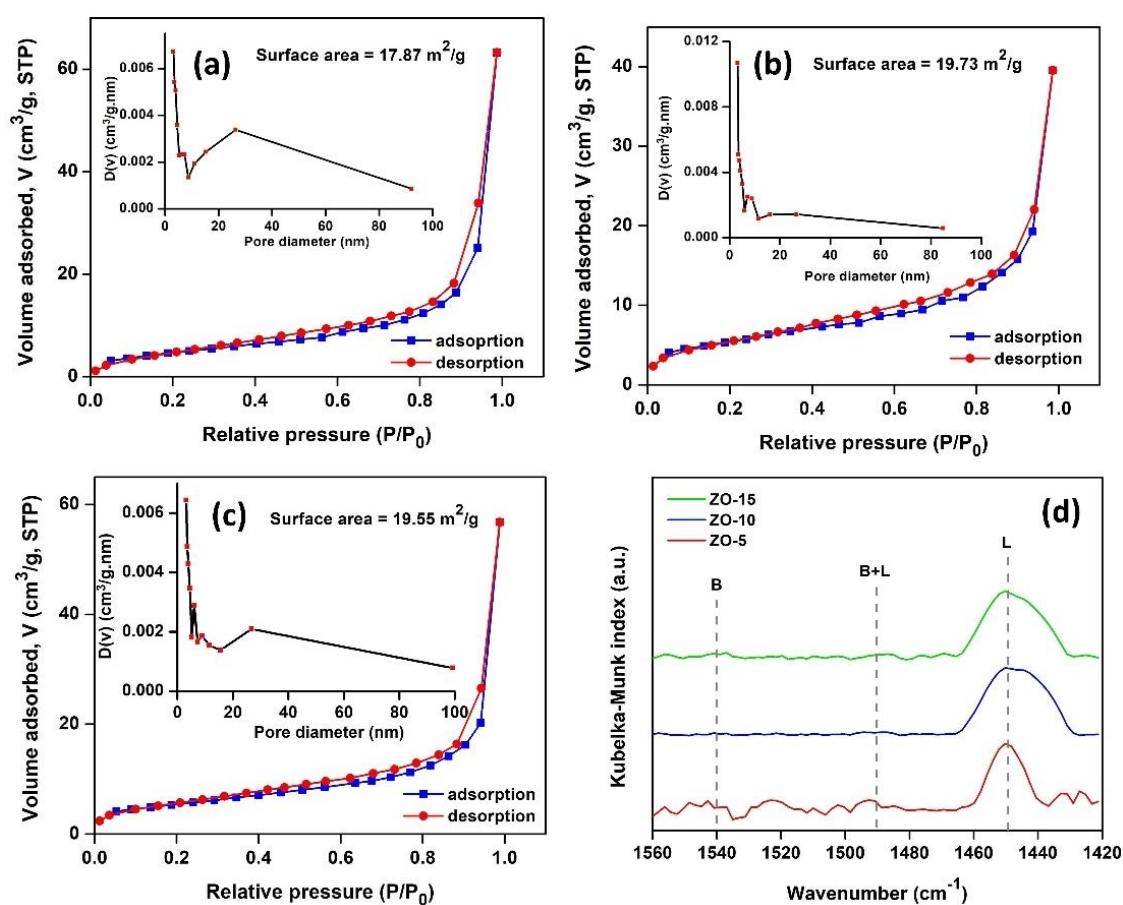


**Figure 3A.6** XPS survey spectra (a), Zn 2p spectra (b) and O 1s spectra (c) of ZnO nanostructures.

The C 1s peak at 284.8 eV appearing as a contamination carbon is used as a reference for all the spectra. The high resolution XPS spectra of the Zn 2p region are shown in Figure

3A.6b. The characteristic doublet peaks of Zn  $2p_{1/2}$  and Zn  $2p_{3/2}$  in this region correspond to Zn<sup>2+</sup> oxidation state [47]. It can be observed from the figure that the binding energies of the Zn 2p components are varying with the increase in hydrothermal time, which could be attributed to various morphologies of the ZnO HNs [48]. This observation corroborates well with the FESEM studies. However, the binding energy (BE) difference between the two Zn 2p components is 23.1 eV which corroborates well with standard reference value of ZnO [49]. Again, the high resolution XPS spectra of the O 1s region are shown in Figure 3A.6c. All the O 1s spectra are deconvoluted into two Gaussian peaks: a low BE peak O<sub>I</sub> and a high BE peak O<sub>II</sub>. O<sub>I</sub> corresponds to O<sup>2-</sup> ions or lattice oxygen in the hexagonal wurtzite structure of ZnO whereas O<sub>II</sub> is related to adsorbed oxygen species onto the surface of the ZnO nanostructures [48, 50].

The porosity and surface area of the ZnO samples are investigated using N<sub>2</sub> sorption experiments. Figure 3A.7a–c shows the N<sub>2</sub> adsorption–desorption isotherms of the ZnO samples and insets correspond to the respective BJH pore size distribution plots.



**Figure 3A.7** N<sub>2</sub> adsorption-desorption isotherms and pore size distribution (inset) of ZO-5 (a), ZO-10 (b), ZO-15 (c) and py-FTIR spectra of the ZnO nanostructures (d).

All the N<sub>2</sub> adsorption-desorption isotherms of the ZnO samples exhibit type IV isotherm with an apparent hysteresis loop at P/P<sub>0</sub> ranging from 0.30 to 0.99 indicative of abundant mesopores [51]. Based on IUPAC classifications, the hysteresis loop of all the ZnO samples resembles a hybrid of H1 and H3 profiles which are associated with the presence of mesopores and slit-shaped pores, respectively [52]. The specific surface area, pore size and pore volume of the samples are presented in Table 3A.2. It can be seen from Table 3A.2 that among the three ZnO samples, ZO-10 and ZO-15 possess higher surface areas compared to ZO-5. The decreased surface area of ZO-5 could be due to the higher agglomeration of the nanoparticles as evident from FESEM results. Nevertheless, the surface areas of all the samples are larger than that of commercial ZnO (4-5 m<sup>2</sup>g<sup>-1</sup>) and other reported ZnO HNs [53].

**Table 3A.2** Physical parameters of ZnO samples obtained from N<sub>2</sub> adsorption-desorption analysis.

Sample	BET surface area (m <sup>2</sup> g <sup>-1</sup> )	Pore volume (cm <sup>3</sup> g <sup>-1</sup> )	Average pore diameter (nm)
ZO-5	17.66	0.096	31.15
ZO-10	19.73	0.057	31.56
ZO-15	19.55	0.083	32.02

Again, the surface acidity of the synthesized samples is assessed by py-FTIR spectroscopy and the results are displayed in Figure 3A.7d. It is known that vibrational modes of pyridine coordinated at Lewis acidic sites (L) appear at ~1445-1460 cm<sup>-1</sup> and those protonated to pyridinium ion at Brønsted acidic sites (B) appear at ~1530-1540 cm<sup>-1</sup> [54]. A combination of both the modes is expected at ~1490 cm<sup>-1</sup>. However, in the present investigation, the py-FTIR bands appear near 1450 cm<sup>-1</sup> for the ZnO nanostructures indicating the presence of Lewis acid sites. The broad bands of ZO-10 and ZO-15 demonstrates higher acidity of these samples compared to ZO-5.

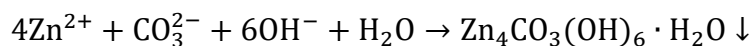
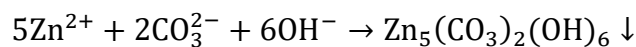
### 3A.1.2 Formation mechanism of ZnO hierarchical nanostructures

Based on the above experimental observations, a possible growth mechanism for the formation of ZnO hierarchical nanostructures is proposed as follows [55, 56]:

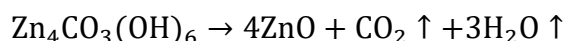
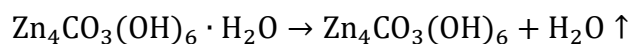
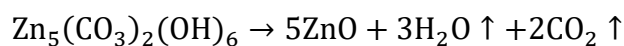
Step I: Thermal decomposition of urea (NH<sub>2</sub>CONH<sub>2</sub>) and generation of CO<sub>3</sub><sup>2-</sup> and 2OH<sup>-</sup> ions.



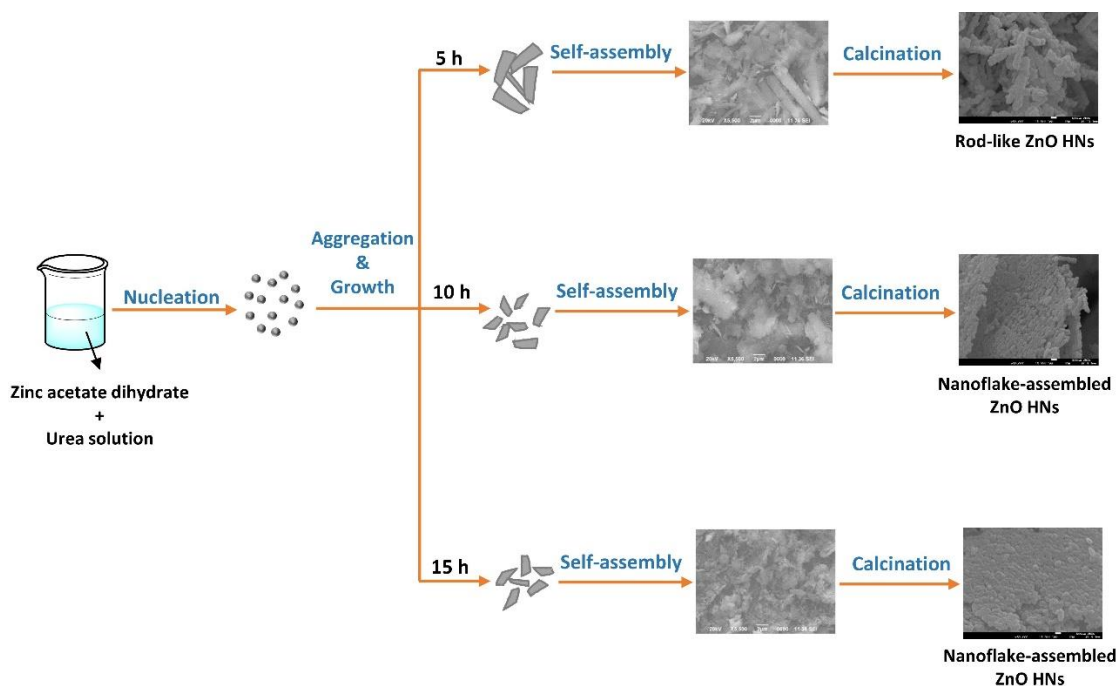
Step II: Precipitation of ZnO precursors ( $\text{Zn}_5(\text{CO}_3)_2(\text{OH})_6$  and  $\text{Zn}_4\text{CO}_3(\text{OH})_6 \cdot \text{H}_2\text{O}$ ) under hydrothermal conditions.



Step III: Formation of ZnO HNs by calcination of ZnO precursors.



A schematic mechanism for the formation and self-construction of ZnO HNs during different stages is illustrated in Scheme 3A.1.



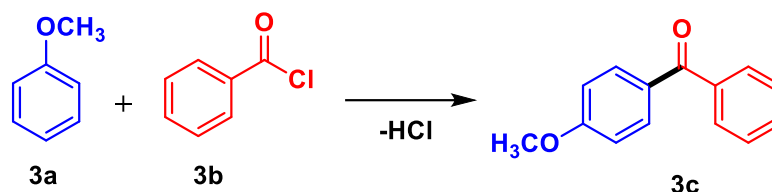
**Scheme 3A.1** Schematic illustration of the formation of ZnO hierarchical nanostructures.

### 3A.1.3 Catalytic activity of ZnO hierarchical nanostructures

The catalytic activity of the synthesized ZnO nanostructures is investigated for the Friedel-Crafts acylation reaction using benzoylation of anisole (3a) with benzoyl chloride (3b) as a model reaction. A blank experiment without catalyst is also conducted which afforded no reaction implying the role of catalyst. To find the optimized condition for obtaining better yields of 4-methoxybenzophenone (3c), the FC reaction is carried out first with ZO-15 nanocatalyst under various reaction conditions as presented in Table

3A.3. It can be observed from the table that the solvent has a significant effect on the reaction.

**Table 3A.3** FC acylation of anisole with benzoyl chloride under various reaction conditions<sup>a</sup>



Entry	Catalyst	Solvent	Temperature (°C)	Time (min)	Yield <sup>b</sup>
1	None	Solvent-free	rt	> 120	n.r
2	ZO-15	Solvent-free	rt	30	72
3	ZO-15	CH <sub>3</sub> NO <sub>2</sub>	rt	30	65
4	ZO-15	CH <sub>2</sub> Cl <sub>2</sub>	rt	20	88
5	ZO-15	CH <sub>3</sub> CN	rt	> 120	trace
6	ZO-15	DMSO	rt	> 120	trace
7	ZO-15	THF	rt	> 120	trace
8	ZO-15	CH <sub>2</sub> Cl <sub>2</sub>	40	15	88
9	ZO-15	CH <sub>2</sub> Cl <sub>2</sub>	60	15	89

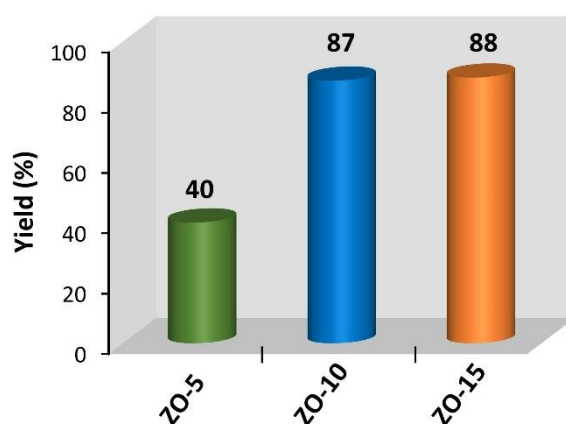
<sup>a</sup>Reaction conditions: anisole (1 mmol), benzoyl chloride (1 mmol), solvent (2.5 mL) and catalyst (20 mol%).

<sup>b</sup>Isolated yields; n.r: no reaction.

The reaction furnishes 72% and 65% yields of 3c under solvent-free condition and CH<sub>3</sub>NO<sub>2</sub>, respectively. Dichloromethane (CH<sub>2</sub>Cl<sub>2</sub>) affords commendable yield of 88% within 20 min. However, for solvents with strong coordination ability such as acetonitrile (CH<sub>3</sub>CN), dimethyl sulfoxide (DMSO) and tetrahydrofuran (THF), only trace products are detected. Therefore, further studies on the effect of temperature on the reaction are performed by employing CH<sub>2</sub>Cl<sub>2</sub> as the solvent. Although the reaction time is reduced with increasing temperature, the obtained yields of 3c are quite comparable. Therefore, the reaction is further screened with various ZnO HNs at room temperature to evaluate their catalytic activity. It is observed from the Figure 3A.8 that all the synthesized ZnO nanostructures are catalytically active for the reaction, suggesting that the Zn<sup>2+</sup>



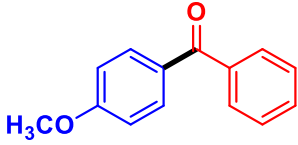
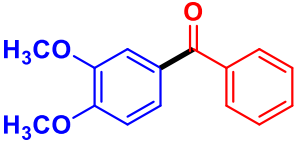
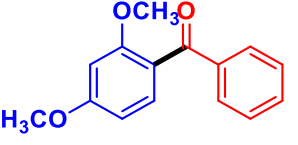
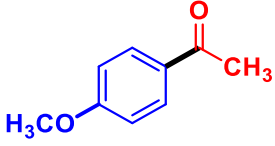
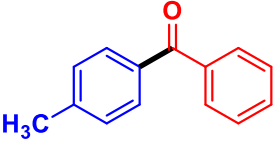
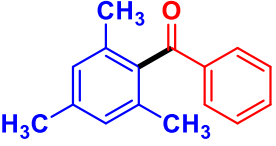


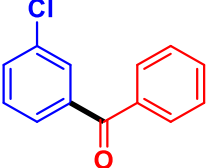
distributed in the sample can act as effective Lewis acid centers for the FC reaction. However, the relatively low yield of ZO-5 may be due to the lower surface area and higher agglomeration of the catalyst. ZO-10 and ZO-15 show relatively high catalytic activities for the acylation reaction. The high activity of the nanoflake assembled HNs of ZO-10 and ZO-15 could be ascribed to synergetic effect of high acidity and surface area which facilitates better adsorption of reactant molecules onto the active sites of the catalysts' surface. Moreover, the diffusion efficiency of organic molecules is enhanced in thin flake-like morphologies as the building blocks are completely accessible by reactant species [57].



**Figure 3A.8** Effect of ZnO HNs on the yield of 4-methoxybenzophenone with reaction conditions: anisole (1 mmol), benzoyl chloride (1 mmol), solvent (2.5 mL) and catalyst (20 mol%).

The acylation of a range of aromatic compounds is also examined, as shown in Table 3A.4, to illustrate the general applicability of ZnO HNs in FC acylation reactions. The arenes with electron-donating  $-\text{CH}_3$  and  $-\text{COCH}_3$  groups could be effectively converted into their corresponding aromatic ketones with considerably high yields (Table 3A.4, entries a–f). The acylation of benzene with benzoyl chloride/acetyl chloride seems more difficult to perform as the aromatic substrate is volatile and less reactive (Table 3A.4, entries g and h). On the other hand, the presence of electron-withdrawing group like  $-\text{Cl}$  on the aromatic ring do not undergo the acylation reaction (Table 3A.4, entry i).

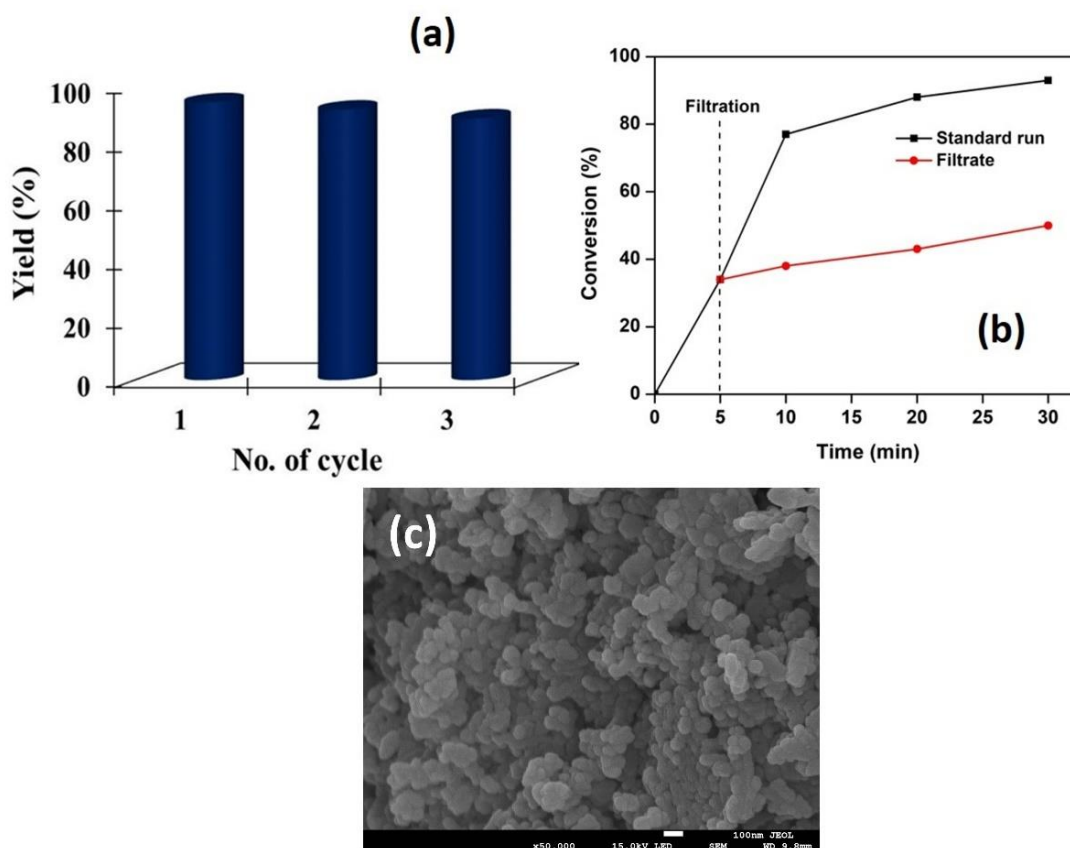
**Table 3A.4** Substrate scope for FC acylation reaction over ZO-15 catalyst<sup>a</sup>.

		
<b>a</b>	<b>b</b>	<b>c</b>
88 %	89 %	87 %
		
<b>d</b>	<b>e</b>	<b>f</b>
90 %	86 %	75 %
		
<b>g</b>	<b>h</b>	<b>i</b>
trace	trace	n.r

<sup>a</sup>Reaction conditions: arene (1 mmol), acid chloride (1 mmol), CH<sub>2</sub>Cl<sub>2</sub> (2.5 mL) and ZO-15 (20 mol%).

n.r: no reaction.

Again, recyclability of catalyst is an important factor in decreasing environmental pollution and reducing the cost of industrial processes. For the recyclability test, three consecutive cycles of catalytic reaction are performed using ZO-15 under optimized conditions and the obtained results are presented in Figure 3A.9. After each run, ZnO nanocatalyst is separated from the reaction mixture by centrifugation, washed with ethanol, dried and employed in a fresh reactant mixture identical to the previous run.



**Figure 3A.9** Recyclability test (a), Hot filtration test (b) of ZO-15 and FESEM image of recovered ZO-15 nanocatalyst after third cycle (c).

As shown in Figure 3A.9a, the high yield of 3c is retained without significant loss of activity up to three consecutive cycles. The minute decrease in activity could be due to the unavoidable trace mechanical loss of catalyst during its separation. Furthermore, a hot filtration test is conducted to investigate the leaching of the ZnO HNs (Figure 3A.9b). After 5 min of the model reaction between anisole and benzoyl chloride, the catalyst is recovered from the reaction mixture by simple filtration, and the reaction is continued for additional 30 min. Slight enhancement of the conversion of benzoyl chloride is observed after separation of the catalyst suggesting that minute amount of leaching of the catalyst has occurred. It is assumed that the reaction of ZnO nanostructures with by-product HCl generates  $\text{ZnCl}_2$ ,  $\text{Zn(OH)}_2$  and/or  $\text{Zn(OH)Cl}$  and destroys the morphology (Figure 3A.9c) [58]. However, the formation of these compounds is endothermic and hence their formation in our condition of room temperature is very low [59].

In summary, we have developed a facile and effective route to synthesize ZnO hierarchical nanostructures. Further, the catalytic activities of the synthesized ZnO hierarchical nanostructures are evaluated for Friedel-Crafts acylation of aromatic compounds. All the synthesized HNs are found to be catalytically active towards the FC acylation reaction at room temperature. Depending on the variation of hydrothermal reaction time in the synthesis, the morphology and surface property of the ZnO HNs changes and as a result shows diverse activity. The HNs synthesized at a hydrothermal time of 10 and 15 h, i.e., ZO-10 and ZO-15 show better catalytic activity towards the FC acylation reaction compared the HNs synthesized using 5 h, i.e., ZO-5. The enhanced activity of ZO-10 and ZO-15 are attributable to their high surface area, acidity and flake-like morphology. The ZnO HNs can also catalyze the acylation reaction without much loss of activity up to three cycles of the reaction. Finally, these features make the ZnO HNs suitable candidate for the catalytic Friedel-Crafts acylation reaction for the synthesis of aromatic ketones.

## **Section 3B: SnO<sub>2</sub> nanoparticles as reusable catalyst for Friedel-Crafts benzylation of anisole**

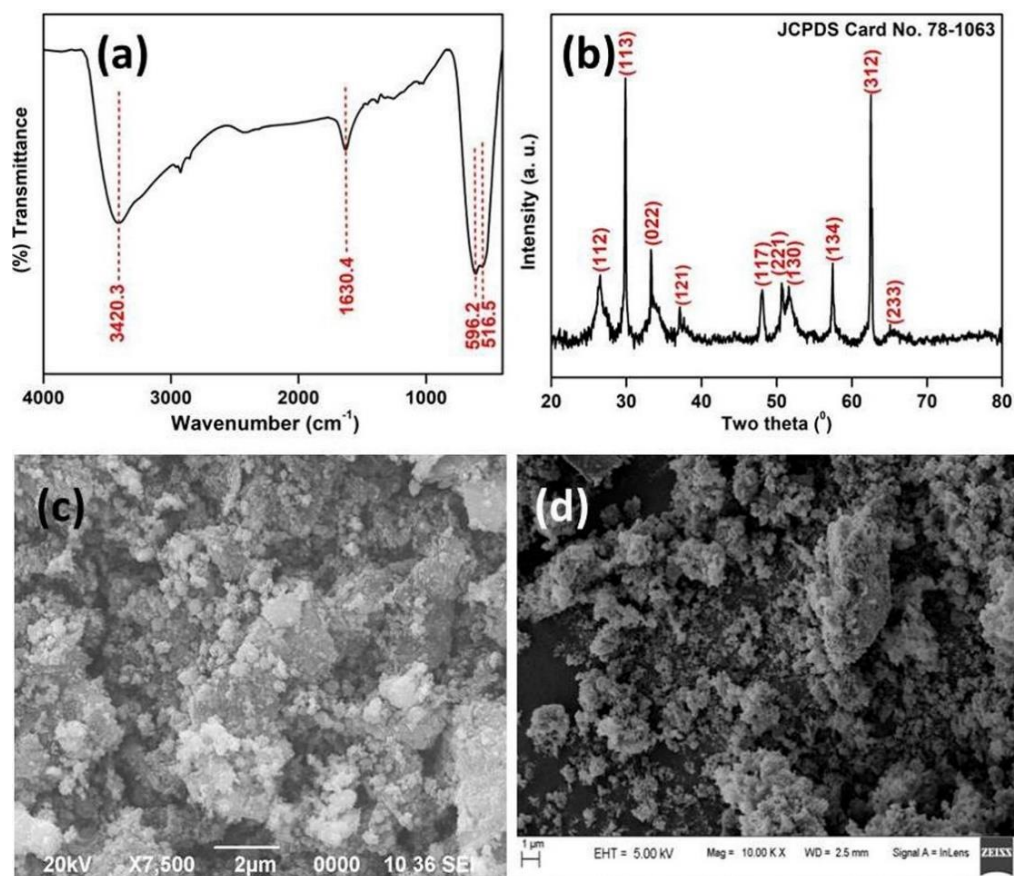
In this section, we have discussed the complete characterization of SnO<sub>2</sub> nanoparticles (NPs) synthesized via solvothermal method using ethanol as solvent. The catalytic activity of the SnO<sub>2</sub> NPs towards the Friedel-Crafts (FC) benzylation of anisole has been discussed herein. The procedures for the synthesis of SnO<sub>2</sub> NPs, characterization techniques and catalytic reactions were described in the Chapter 2.

### **3B.1 Results and discussion**

#### ***3B.1.1 Characterization of SnO<sub>2</sub> nanoparticles***

The FTIR spectrum (Figure 3B.1a) of the synthesized material shows two absorption bands centered at 596.2 and 516.5 cm<sup>-1</sup> that can be assigned to O–Sn–O and Sn–O vibrations, respectively. The presence of absorption bands at ~3420.3 cm<sup>-1</sup> and 1630.4 cm<sup>-1</sup> can be attributed to stretching and bending vibrations of surface hydroxyl groups of molecular water, respectively. The crystalline property of the sample is characterized by XRD as shown in Figure 3B.1b. All the diffraction peaks in the XRD pattern can be indexed to orthorhombic SnO<sub>2</sub> in accordance with the JCPDS card no. 78-1063. No secondary phase is observed in the synthesized SnO<sub>2</sub>, revealing the high purity of the sample. Usually, SnO<sub>2</sub> crystallizes in its tetragonal rutile structure in hydro/solvothermal treatment [60–63]. In our study, the presence of solvent (ethanol) with an external temperature of 100°C leads to the formation of orthorhombic SnO<sub>2</sub> phase. It may be due to the presence of ethanol as the solvent that can control the internal temperature/pressure of the reaction in which it occurs.

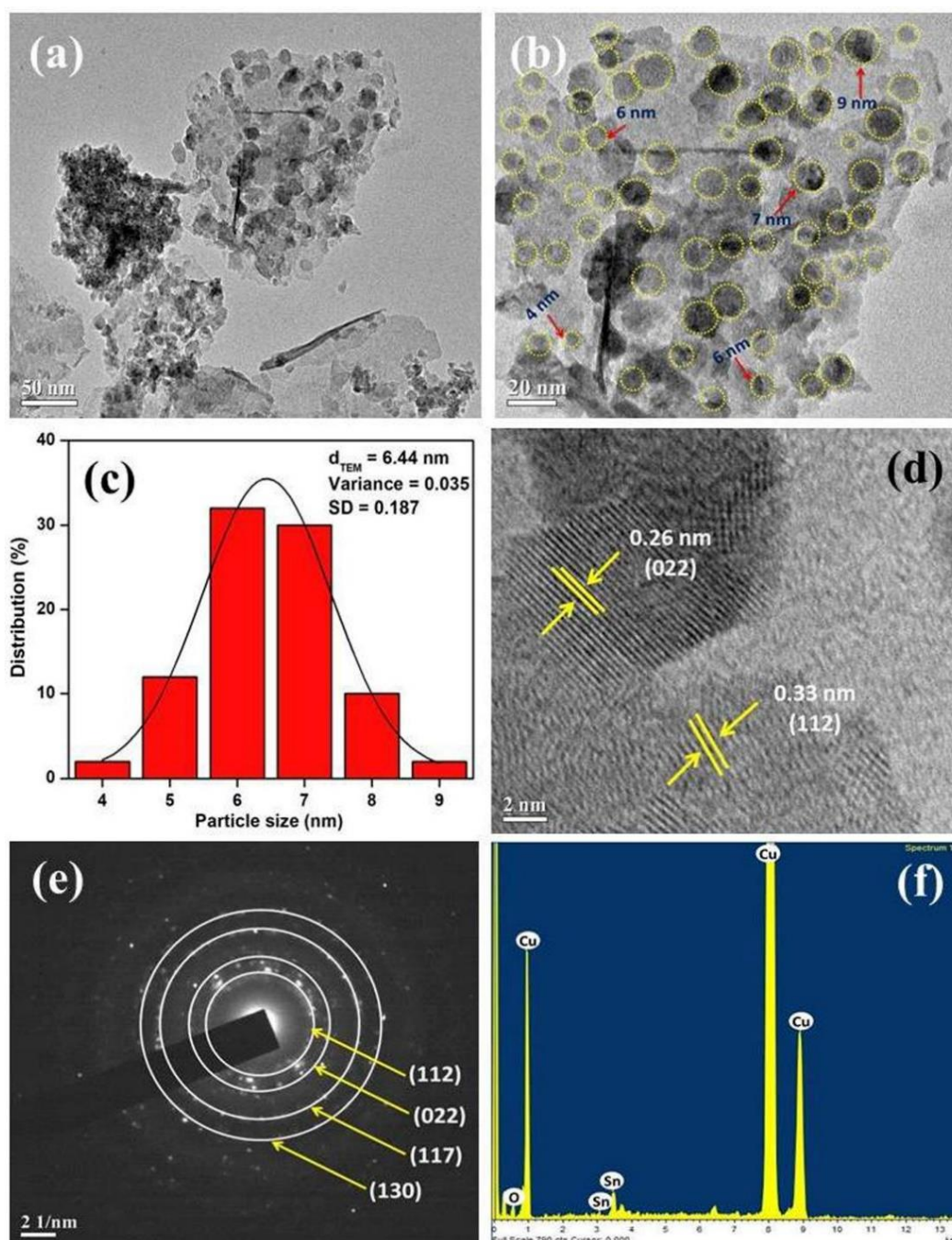
The morphology and surface topography of the synthesized SnO<sub>2</sub> is characterized by microscopic investigations such as SEM, FESEM, and TEM techniques. Figure 3B.1c shows the SEM micrograph of the sample. From the micrograph, it is observed that the size of the individual particles is very small and the aggregation of particles takes place. Moreover, the FESEM image (Figure 3B.1d) shows the presence of irregularly shaped small NPs due to the agglomeration of very tiny particles.



**Figure 3B.1** FTIR spectrum (a), XRD pattern (b), SEM image (c) and FESEM image (d) of as-synthesized SnO<sub>2</sub> NPs.

The morphology of the sample is further determined by TEM analysis and the results are presented in Figure 3B.2. The TEM study shows the formation of fine SnO<sub>2</sub> NPs with almost spherical in shape and irregular sizes (Figure 3B.2(a, b)). The particle size distribution of SnO<sub>2</sub> NPs shows that almost 60% of the particles belong to the size range of 6–7 nm with an average particle diameter of 6.44 nm (Figure 3B.2c). In hydrothermal treatment (without a solvent), SnO<sub>2</sub> generally forms nanostructures with different shapes and sizes rather than tiny NPs [62, 64]. However, in our study, the formation of SnO<sub>2</sub> NPs with a size almost less than 7 nm is observed. Again, this may be due to the presence of ethanol along with water during the synthesis process [65]. It is observed that solvent i.e., ethanol plays a major role in the crystalline and morphological properties of the as-synthesized SnO<sub>2</sub> that leads to change in its textural property. Therefore, an increase in surface area is expected for the as-synthesized SnO<sub>2</sub> NPs than SnO<sub>2</sub> nanostructures synthesized by simple hydrothermal treatment.

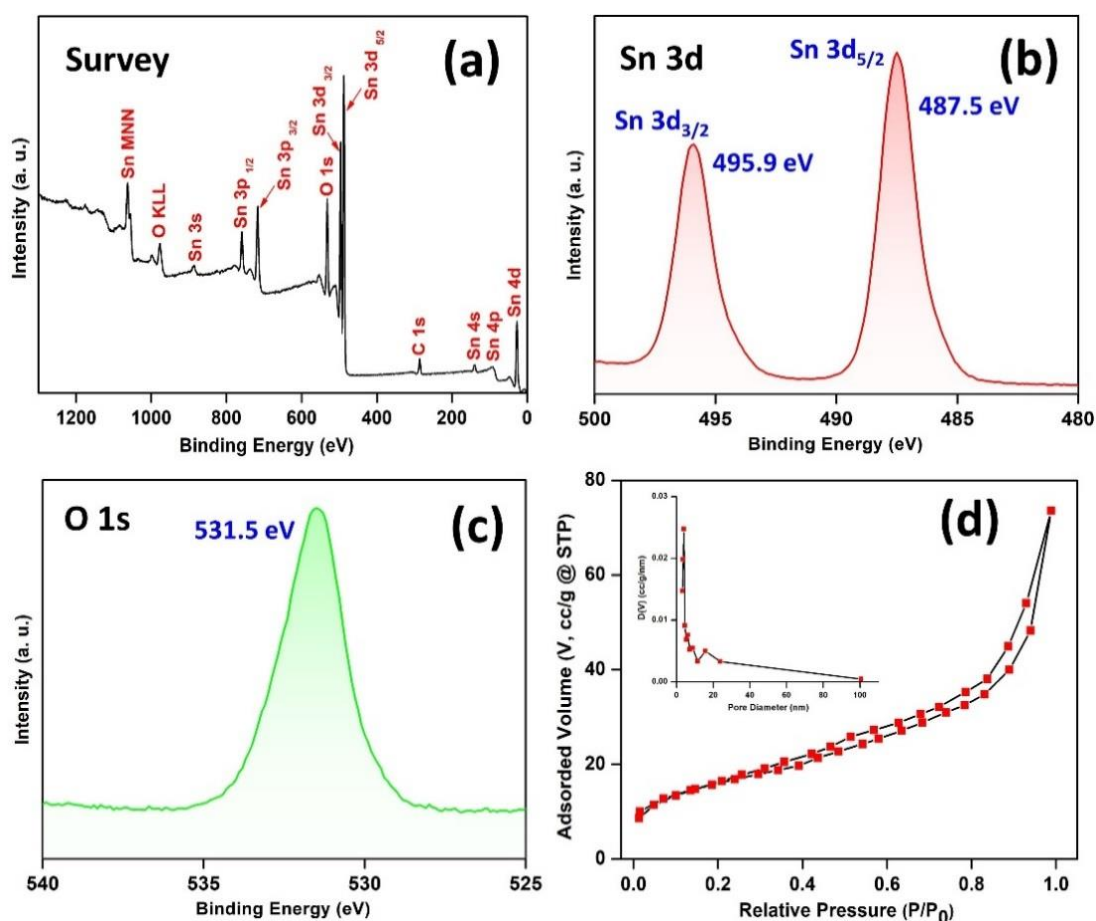




**Figure 3B.2** TEM images at different resolution (a, b), particle size distribution (c), HRTEM image (d), SAED pattern (e) and EDS (f) of the synthesized SnO<sub>2</sub> NPs.

As displayed in Figure 3B.2d, the interplanar distances of 0.26 nm and 0.33 nm are indexed to (022) and (112) planes of orthorhombic SnO<sub>2</sub>. Again, the selected area electron diffraction (SAED) measurement of the sample (Figure 3B.2e) demonstrates that the nanoparticles are highly crystalline in nature with four significant well resolved rings corresponding to (112), (022), (117) and (130) lattice planes of SnO<sub>2</sub> NPs (Figure 3B.2d). The energy dispersive X-ray spectroscopic (EDS) analysis (Figure 3B.2f) of the

sample suggests the occurrence of Sn and O signals devoid of any other element (Cu peaks in the spectrum are due to background from copper TEM grid).



**Figure 3B.3** XPS survey (a); Sn 3d (b); O 1s (c) and BET isotherm (d) of the as-synthesized SnO<sub>2</sub> sample; inset (d): pore size distribution curve of the respective sample.

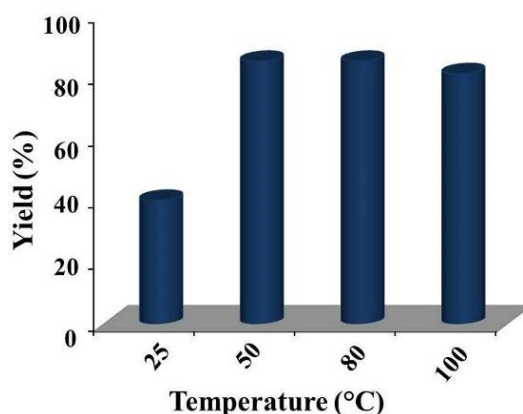
The chemical state of SnO<sub>2</sub> is further investigated using X-ray photoelectron spectroscopy (XPS). As shown from the XPS spectrum, the SnO<sub>2</sub> NPs only show emissions of Sn, O and C with no other elements (Figure 3B.3a). The C 1s peak arises due to the use of carbon tape to mount the powder sample. The peaks at 487.5 eV and 495.9 eV in the Sn 3d spectrum (Figure 3B.3b) can be attributed to Sn 3d<sub>5/2</sub> and Sn 3d<sub>3/2</sub>, respectively that arises due to Sn<sup>4+</sup> of SnO<sub>2</sub>. The peak at 531.5 eV in the O 1s spectrum (Figure 3B.3c) can be assigned to O<sup>2-</sup> species of SnO<sub>2</sub> crystal lattice [64].

Further, the textural property of SnO<sub>2</sub> NPs is assessed by nitrogen adsorption/desorption analysis and presented in Figure 3B.3c. The isotherm belongs to type IV with a combination of H1 and H3 hysteresis loops, that is a typical characteristic of mesoporous materials [66]. The upper closer point of the hysteresis loop appears at a

substantially higher value ( $P/P_0 = 0.90$ ) suggesting the mesoporosity of the sample. The obtained surface area for the synthesized sample is  $56.19 \text{ m}^2\text{g}^{-1}$ , which is consistent with literature reports on metal oxide nanoparticles [66, 67]. This is also in accordance with the TEM results of as-synthesized  $\text{SnO}_2$  NPs. Moreover, a pore volume of  $0.099 \text{ cm}^3\text{g}^{-1}$  and pore diameter of 3.96 nm is calculated using the BJH method which again confirms the mesoporosity of the sample.

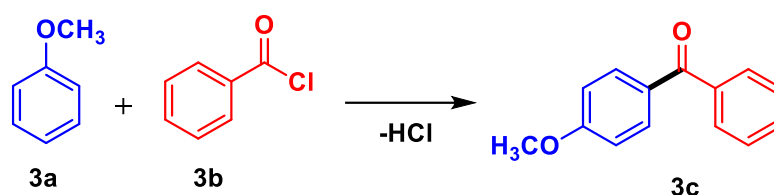
### 3B.1.2 Catalytic activity of $\text{SnO}_2$ nanoparticles

The catalytic activity of the synthesized  $\text{SnO}_2$  NPs is evaluated by performing the Friedel-Crafts benzylation of anisole. To determine the optimum reaction conditions for achieving a high yield of product, we examine the effect of various reaction parameters to yield corresponding aromatic ketone, 4-methoxybenzophenone. The reaction is carried out under various temperatures ranging from  $25^\circ\text{C}$  to  $100^\circ\text{C}$  and the results are shown in Figure 3B.4.



**Figure 3B.4** Effect of temperature on the yield of product of the reaction. Reaction conditions: anisole (1 mmol), benzoyl chloride (1 mmol) and catalyst (5 mol%).

The yield of aromatic ketone gradually increases with increasing the reaction temperature up to  $50^\circ\text{C}$ . However, no appreciable difference in the catalytic performance is observed upon further increasing the reaction temperature. The results suggest that  $\text{SnO}_2$  nanoparticle can catalyze the aforementioned reaction at  $50^\circ\text{C}$  effectively. Therefore,  $50^\circ\text{C}$  is considered as an optimum temperature for the mentioned reaction. It is noteworthy that the reaction does not proceed without the nanocatalyst signifying the role of the catalyst in reaction (Table 3B.1, entry 1).

**Table 3B.1** Screening of catalytic effect for Friedel-Crafts acylation reaction<sup>a</sup>

Entry	Catalyst	Amount of catalyst		
		(mol %)	Solvent	Yield <sup>b</sup> (%)
1	No catalyst	-	Solvent-free	No reaction
2	AlCl <sub>3</sub> (anhyd.)	10	Solvent-free	55
3	FeCl <sub>3</sub> (anhyd.)	10	Solvent-free	74
4	ZnCl <sub>2</sub> (anhyd.)	10	Solvent-free	34
5	SnO <sub>2</sub> NPs	3	Solvent-free	30
6	SnO <sub>2</sub> NPs	4	Solvent-free	52
7	SnO <sub>2</sub> NPs	5	Solvent-free	85
8	SnO <sub>2</sub> NPs	6	Solvent-free	80
9	SnO <sub>2</sub> NPs	5	CH <sub>3</sub> NO <sub>2</sub>	65
10	SnO <sub>2</sub> NPs	5	ACN	34
11	SnO <sub>2</sub> NPs	5	EA	25
12	SnO <sub>2</sub> NPs	5	THF	65
13	SnO <sub>2</sub> NPs	5	DCM	20

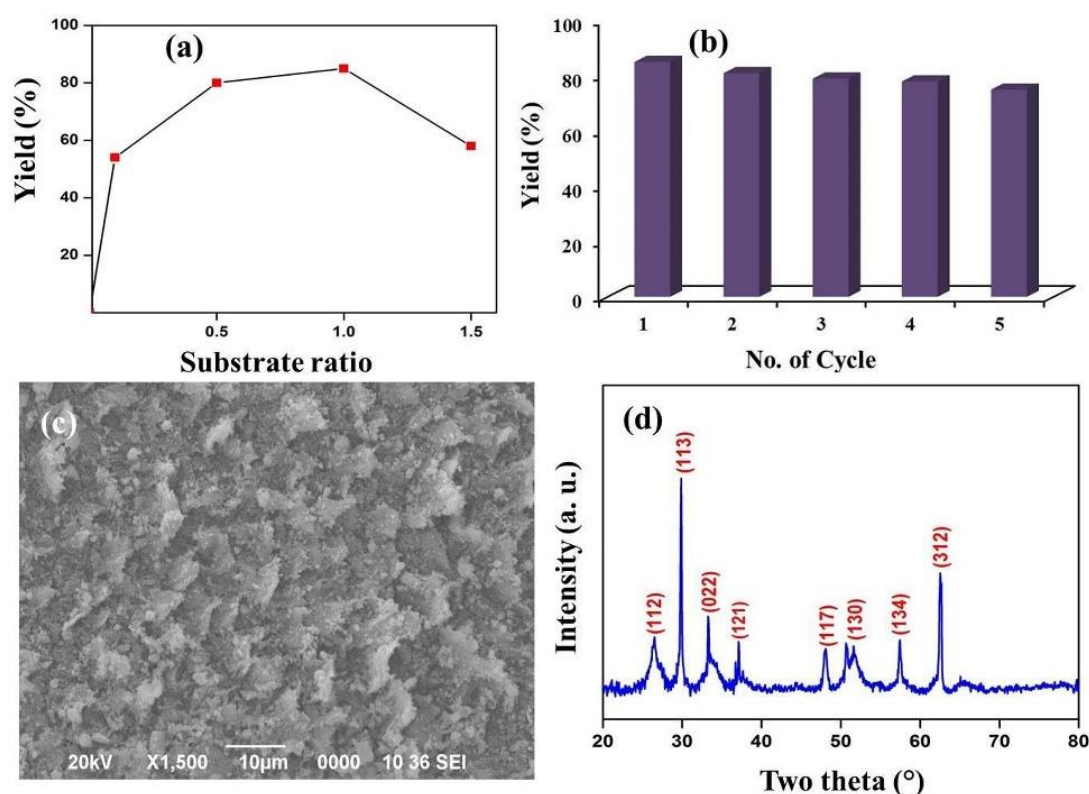
<sup>a</sup>Reaction conditions: Anisole (1 mmol) and Benzoyl chloride (1 mmol) at 50°C.

<sup>b</sup>Isolated yield.

We have also tested the catalytic effect of some conventional catalysts such as anhydrous AlCl<sub>3</sub>, FeCl<sub>3</sub>, and ZnCl<sub>2</sub> catalysts for comparison with the present protocol (Table 3B.1, entries 2–3). However, the benzoylation of anisole requires a very high amount of these catalysts and subsequently give low amounts of corresponding yields. Further, the reaction is tested using SnO<sub>2</sub> NPs with varying amounts of catalyst (Table 3B.1, entries 5–8). It can be seen from Table 3B.1 that the yield of the product increases with increasing amount of catalyst from 3 mol% to 5 mol%. Further increase in catalyst concentration to 6 mol% did not result in enhancement of the product yield, which may

be due to the fact that higher concentrations of catalysts make the reaction mixture more viscous thereby leading to resisted mass transfer. Likewise, the effect of various solvents on the reaction is scrutinized (Table 3B.1, entries 9–13). Although it is observed that the reaction proceeds smoothly in the presence of these solvents, yet low yields are attained in comparison to that of solvent-free conditions. Therefore, we have found SnO<sub>2</sub> NPs in solvent-free conditions exhibit high catalytic activity for the benzylation reaction.

Again, we have investigated the influence of benzoyl chloride to anisole mole ratio by varying it from 0.1 to 1.5 with 5 mol% of catalyst at 50°C (Figure 3B.5a).



**Figure 3B.5** Effect of benzoyl chloride to anisole mole ratio on the yield of product of the reaction (a); Recyclability test (b); SEM image (c) and XRD pattern (d) of the SnO<sub>2</sub> NPs after fifth run, respectively of Friedel-Crafts benzylation of anisole. Reaction conditions: Catalyst (5 mol%) and temperature 50°C.

It is seen from the Figure 3B.5a that the yield of aromatic ketone increases upon increasing the mole ratio from 0.1 to 1 and decreases after further increasing the mole ratio. Therefore, it can be concluded that best result is obtained at 50°C with SnO<sub>2</sub> catalyst (5 mol%) using anisole to benzoyl chloride mole ratio of 1 under solvent-free condition.

Further, the recyclability test of the SnO<sub>2</sub> nanocatalyst is performed for consecutive reactions with fresh anisole and benzoyl chloride. The catalyst is recovered from the reaction mixture by centrifugation, washed with ethanol, dried, and then used for further catalytic cycle by addition of fresh reactants identical to initial run (Figure 3B.5b). A slight decrease in the yield of the product is observed after completing each run. This minute drop could be attributed to catalyst loss during the separation process. The as-synthesized SnO<sub>2</sub> NPs exhibit good catalytic activity with high stability up to fifth consecutive cycle (Figure 3B.5(c, d)). Finally, all the results indicate that the SnO<sub>2</sub> NPs synthesized via ethanol mediated solvothermal route can be effectively used as an attractive contender for the Friedel-Crafts benzylation of anisole.

In summary, SnO<sub>2</sub> NPs are synthesized via a facile solvothermal method using ethanol as a solvent. The synthesized SnO<sub>2</sub> is characterized by FTIR, XRD, SEM, FESEM, TEM/HR-TEM, XPS, Raman spectroscopy, and BET surface area analysis. XRD profile shows that the synthesized oxide adopts an orthorhombic SnO<sub>2</sub> structure. TEM study confirms the formation of nanoparticles with an average size 6.44 nm. The nature of the solvent present in the synthesis process greatly affects the morphological texture of SnO<sub>2</sub> nanomaterial. Further, the synthesized SnO<sub>2</sub> NPs are employed for the Friedel-Crafts benzylation of anisole to yield corresponding 4-methoxybenzophenone as a product. The results indicate that the synthesized SnO<sub>2</sub> catalyze the reaction very effectively with recyclability up to five successive cycles. It also indicates that SnO<sub>2</sub> NPs can be effectively used as an attractive alternative for the synthesis of aromatic ketones.



### **Section 3C: Regioselective Friedel-Crafts acylation reaction using single crystalline and ultrathin nanosheet assembly of scrutinyite-SnO<sub>2</sub>**

Herein, we have discussed the synthesis and characterization of single crystalline and ultrathin 2D nanosheet (NS) assembly of scrutinyite-SnO<sub>2</sub> through a template-free solvothermal method. The catalytic activity of the SnO<sub>2</sub> NS assembly towards the regioselective Friedel-Crafts acylation has been discussed. The procedures for the synthesis of SnO<sub>2</sub> NS assembly, characterization techniques and catalytic experiments are described in the Chapter 2.

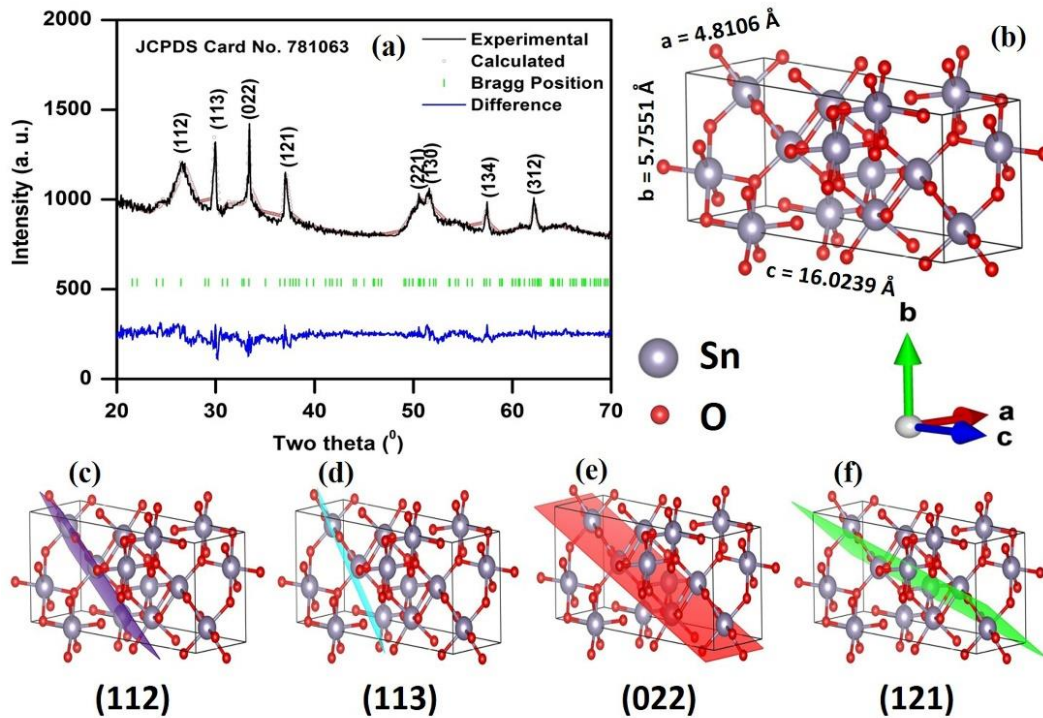
#### **3C.1 Results and discussion**

##### ***3C.1.1 Characterization of the SnO<sub>2</sub> nanocatalyst***

At first, FTIR spectroscopic study of the as-synthesized sample confirms the formation of metal oxide with strong absorption bands located at mid and far regions of IR spectra (Figure A.2 of Appendix). The mid-FTIR spectrum (Figure A.2a) shows three intense bands at around 540.2, 585.6 and 692.0 cm<sup>-1</sup> due to the stretching and bending vibration of Sn–O bond in orthorhombic SnO<sub>2</sub> lattice. The presence of a broad band at 3415.1 cm<sup>-1</sup> and a weak band at 1643.2 cm<sup>-1</sup> may be due to the stretching and bending vibration of hydroxyl groups of Sn–OH or coordinated H<sub>2</sub>O molecules of SnO<sub>2</sub> lattice [68]. In far-FTIR spectrum (Figure A.2.b), some weaker broad bands located around 150–300 cm<sup>-1</sup> is observed that may be due to a few combination modes of bending and torsional vibrations of Sn–O bond [69]. No other absorption and inverse absorption bands are observed in the spectrum indicating the absence of defects associated with oxygen vacancies or tin interstitials and molecular SnCl<sub>2</sub>, respectively [68]. Thus, this FTIR study confirms the formation of SnO<sub>2</sub> through the solvothermal treatment of tin chloride dihydrate with NaOH.

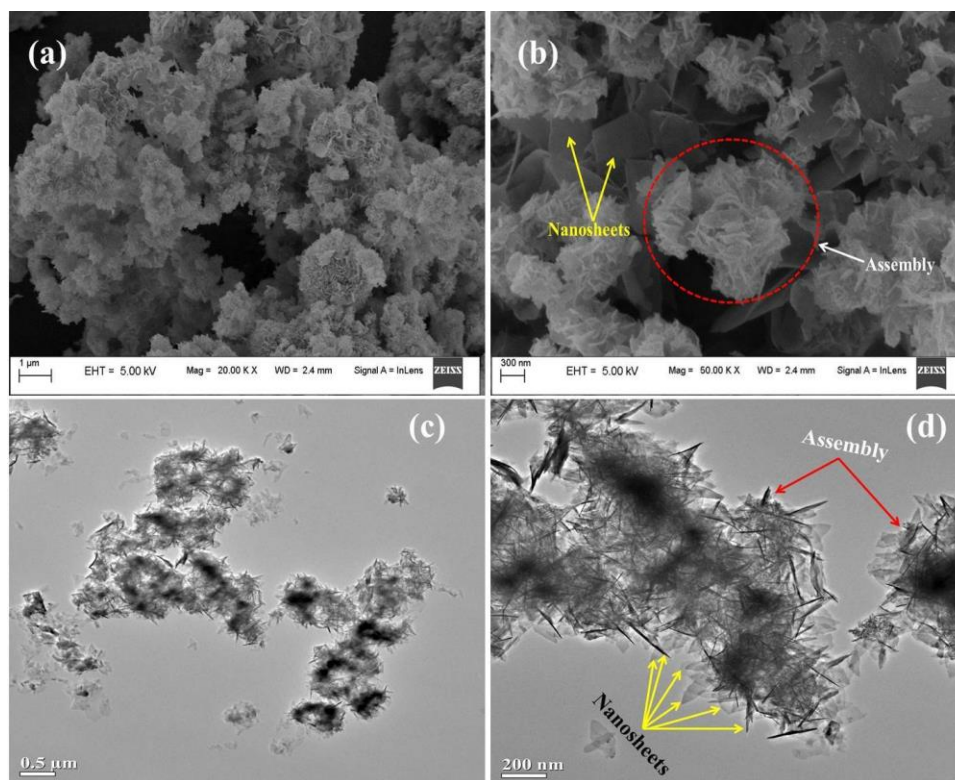
The powder XRD analysis is carried out for the as-synthesized sample and results show the X-ray diffraction peaks at  $2\theta = 26.9, 29.7, 33.4, 37.2, 47.2, 50.4, 51.8, 57.1, 60.8, 62.0, 65.3, 70.1$  and  $78.1^\circ$  that are assigned to diffractions of (112), (113), (022), (121), (117), (221), (130), (134), (208), (312), (233), (228) and (240) crystal planes, respectively of orthorhombic i.e. scrutinyite-SnO<sub>2</sub> crystal structure correctly match with JCPDS Card No. 78-1063 (Figure 3C.1a). Rietveld refinements (Figure 3C.1a) are also carried out using the same powder X-ray diffraction data and found that all the

diffraction peaks are indexed to orthorhombic (scrutinyite) crystal phase of SnO<sub>2</sub> with space group Pbcn (No. 60). Table A.1 of Appendix represents all the lattice and structure parameters of the scrutinyite-SnO<sub>2</sub> sample. There are no oxygen vacancies in the SnO<sub>2</sub> sample confirming the complete formation of scrutinyite-Sn(IV)O [69].



**Figure 3C.1** Results of the Rietveld refinement of the XRD pattern (a), corresponding unit cell (b) and crystallographic planes (c–f) of the scrutinyite-SnO<sub>2</sub>.

Again, crystallite size of the SnO<sub>2</sub> sample is calculated considering the full width at half-maximum (FWHM) of the first four high intense XRD peaks at  $2\theta = 26.9, 29.7, 33.4$  and  $37.2^\circ$  corresponding to (112), (113), (022) and (121) crystal planes, respectively. The crystallite sizes of the (112), (113), (022) and (121) planes of as-synthesized SnO<sub>2</sub> sample are found to be 12.2, 26.9, 71.2 and 23.8 nm, respectively. The crystallite size of (022) plane is found much larger than the other planes, suggesting the main growth of as-synthesized SnO<sub>2</sub> crystallites in the [011] direction. The result means that the main surface of the SnO<sub>2</sub> sample is predominantly contributed by the (022) plane or/and parallel planes in the [011] direction. Consequently, the growth of crystallites of SnO<sub>2</sub> sample perpendicular to [011] direction i.e., in [100] direction must be slow which means the planes in [100] direction or/and the parallel planes of (100) plane have minor contribution to the main surface of SnO<sub>2</sub> sample.



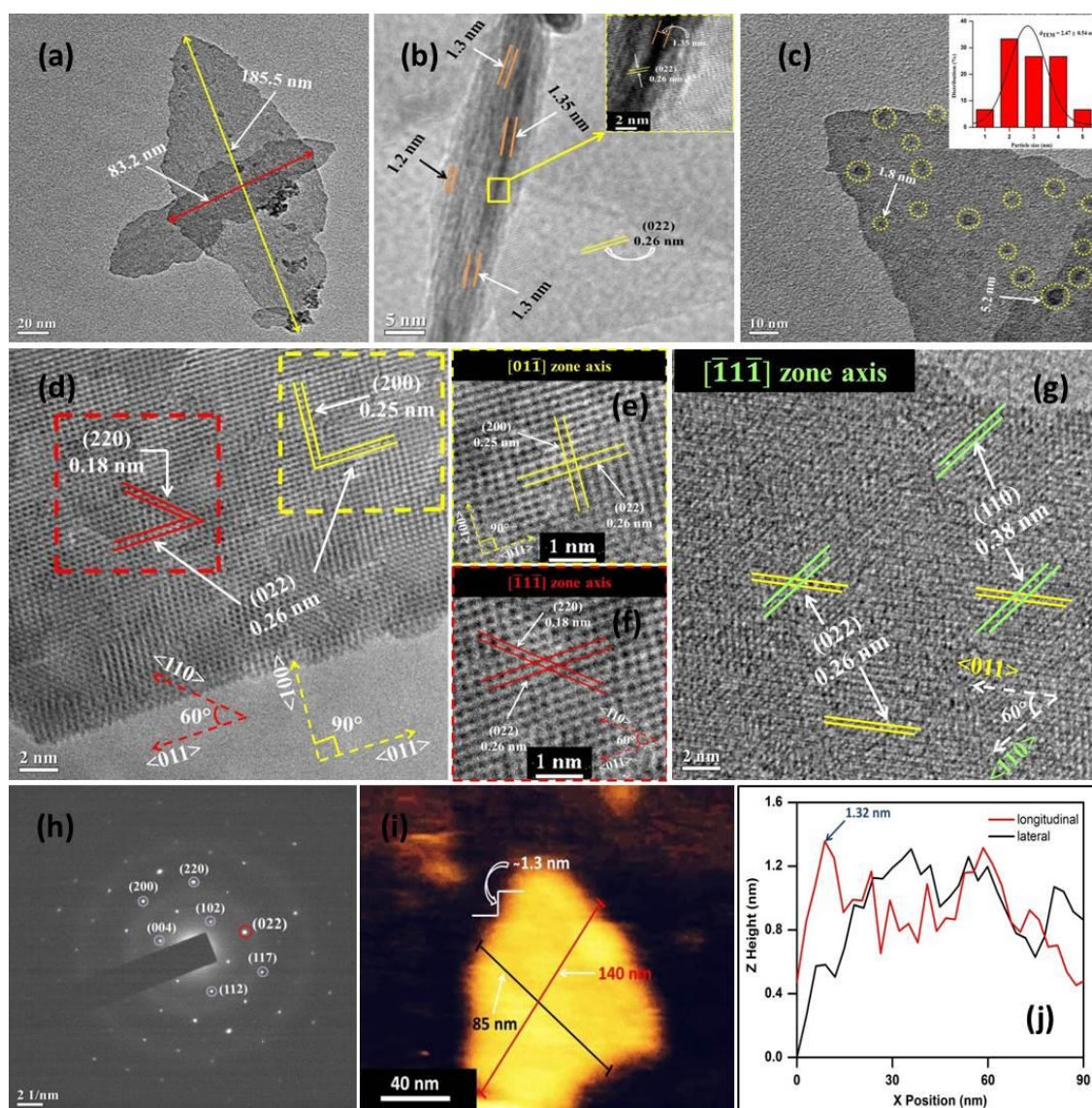
**Figure 3C.2** FESEM (a,b) and low magnified TEM (c,d) images of synthesized scrutinyite-SnO<sub>2</sub> in different resolutions.

The morphology and structural/compositional details of the synthesized scrutinyite-SnO<sub>2</sub> have been studied by SEM/FESEM and TEM analyses. SEM images (Figure A.2(c, d)), FESEM images (Figure 3C.2(a, b)) and TEM images (Figure 3C.2(c, d)) confirm the formation of SnO<sub>2</sub> NSs and assembly of such nanosheets with almost dendritic like morphology. More information about the SnO<sub>2</sub> NSs and its assembly is collected by a series of TEM/HRTEM investigations (Figure 3C.3a–h). The size of the SnO<sub>2</sub> nanosheets is found to be non-uniform with longitudinal dimensions almost 120–200 nm and lateral dimensions 50–100 nm (Figure 3C.3a). The thickness i.e., cross-sectional dimension of SnO<sub>2</sub> NSs is determined by focusing TEM/HRTEM investigation on the edge of the nanosheets assembly. The completely transparent fringe-like regions indicate planar sheets parallel to copper grid and quite dark wire-like regions resemble the sheets perpendicular to the grid (Figure 3C.3b). The measured widths of very dark wire-like regions are found to be 1.2–1.35 nm that confirms the formation of ultrathin NSs (Figure 3C.3b). The planar sheet also clearly displays lattice fringes with spacing of 0.26 nm corresponding to (022) plane of scrutinyite-SnO<sub>2</sub> (Figure 3C.3b). Again, a particularly magnified area of the HRTEM image distinctively shows the lattice fringes

( $d_{022}^{SnO_2} = 0.26$  nm) over the planar nanosheet of scrutinyite-SnO<sub>2</sub> (inset in Figure 3C.3b). Moreover, the nanosheets are formed by strong aggregation and oriented attachment of various tiny particles of a few nano diameters (slightly visible on the top flat surface of the sheet) (Figure 3C.3c). The average diameter of the particles is calculated and found *ca.* 2.47 nm (inset in Figure 3C.3c).

As of yet, the assembly of scrutinyite-SnO<sub>2</sub> formed by ultrathin nanosheets that are made of oriented attachment of tiny particles have been found under TEM/HRTEM investigation. Thereafter, the high resolution TEM investigation is performed for the collection of in-depth information on SnO<sub>2</sub> NSs (Figure 3C.3d–g). Two different zonal areas highlighted with yellow and red color square box corresponding to  $[01\bar{1}]$  and  $[\bar{1}1\bar{1}]$  zone axis, respectively are observed on the surface of a nanosheet (Figure 3C.3d–f). A distinctive set of planes matching with (022) and (200) lattice planes of scrutinyite-SnO<sub>2</sub> at an angle of 90° in between having lattice fringes ( $d_{022}^{SnO_2} = 0.26$  nm) and ( $d_{200}^{SnO_2} = 0.25$  nm), respectively in the  $[01\bar{1}]$  zone axis is clearly visible (highlighted yellow color square box of Figure 3C.3(d, e)). Another set of planes matching with (022) and (220) lattice planes of scrutinyite-SnO<sub>2</sub> making an angle of 60° in between with fringes ( $d_{022}^{SnO_2} = 0.26$  nm) and ( $d_{220}^{SnO_2} = 0.18$  nm), respectively in the  $[\bar{1}1\bar{1}]$  zone axis is also observed (highlighted red color square box of Figure 3C.3(d, f)). Another zonal area with a set of planes matching with (022) and (110) lattice planes of scrutinyite-SnO<sub>2</sub> at an angle of 60° in between having lattice fringes ( $d_{022}^{SnO_2} = 0.26$  nm) and ( $d_{110}^{SnO_2} = 0.38$  nm), respectively is also viewed in the  $[\bar{1}1\bar{1}]$  zone axis of a different portion of the nanosheet (Figure 3C.3g). From the HRTEM investigation, the lattice plane (022) corresponding to the {022} facet of scrutinyite-SnO<sub>2</sub> ( $d_{022}^{SnO_2} = 0.26$  nm) in [011] direction predominantly contributed on the main surface of the NSs along with two other exposed planes (220) and (110) in [110] direction at an angle of 60° to the (022) plane. Moreover, a lattice plane (200) corresponding to the {200} facet in [100] direction at an angle of 90° to the (022) plane also contributes minutely. These results are consistent with the XRD results by confirming the (022) lattice plane as the main exposed crystal plane of the scrutinyite-SnO<sub>2</sub> NSs suggesting predominant growth and orientation of the SnO<sub>2</sub> crystallites in [011] direction with least contribution of (200) lattice plane in [100] direction.





**Figure 3C.3** Morphological and topological characterizations for scrutinyite-SnO<sub>2</sub> NSs assembly. Low-magnification TEM image (a) representing nanosheets, HRTEM image (b) of nanosheets assembly on the edge region (inset shows high magnified image of the yellow square box portion), Low-magnification TEM image (c) of a portion of nanosheet displaying the aggregation and attachment of tiny particles (slightly visible on the top flat surface of the sheet) (inset shows the corresponding particles size distribution), HRTEM image (d) of a nanosheet having two different zonal area (yellow and red color square box corresponding to  $[01\bar{1}]$  and  $[\bar{1}1\bar{1}]$  zone axis, respectively), high magnified HRTEM image of yellow color square box corresponding to  $[01\bar{1}]$  (e) and red color square box corresponding to  $[\bar{1}1\bar{1}]$  (f) zone axis, HRTEM image (g) of a different portion of the nanosheet displaying  $[\bar{1}1\bar{1}]$  zone axis, SAED analysis (h) of the nanosheet, AFM image

(i) of the SnO<sub>2</sub> nanosheet after strong ultrasonic treatment, corresponding height profiles (j) from AFM analysis of the SnO<sub>2</sub> nanosheet.

Further, SAED analysis of the nanosheet shows a spotty pattern revealing the pure and single crystalline nature of the synthesized SnO<sub>2</sub> NSs (Figure 3C.3h). The lattice planes (004), (102), (112), (022), (220), (200) and (117) of scrutinyite-SnO<sub>2</sub> are clearly indexed by the bright spots in the SAED pattern. The higher brightness of (022) spot (red color circle) in the pattern confirms more exposure of (022) lattice plane in the SnO<sub>2</sub> nanosheets which is again in agreement with HRTEM and XRD observation. Again, the thickness of the SnO<sub>2</sub> nanosheet can be further characterized by AFM analysis (Figure 3C.3(i, j)). The AFM image depicts a thickness *ca.* 1.3 nm along with longitudinal and lateral dimension of the NS about 140 and 85 nm, respectively (Figure 3C.3i). The corresponding height profiles show slight roughness in surface of the NS with a height in the range of 0.7–1.32 nm and a maximum height of ~1.32 nm (Figure 3C.3j). The result of AFM analysis strongly confirms the formation of ultrathin NS which is in good agreement with the HRTEM observation.

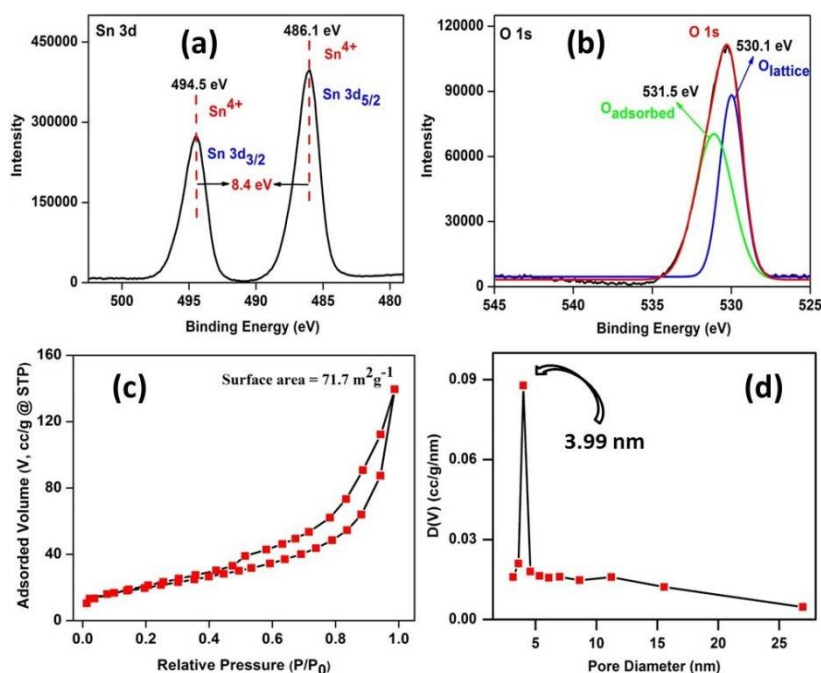
Further, we have conducted Raman spectroscopic and XPS analysis on the single crystalline and ultrathin SnO<sub>2</sub> NS assembly (Figure A.3 of Appendix and Figure 3C.4). Basically, Raman spectroscopy is interrelated with the XRD. However, in contrast to XRD, the number of atoms per unit cell provides the possible phonon modes in Raman spectroscopy. As the primitive cell of scrutinyite-SnO<sub>2</sub> contains 12 atoms, one should achieve a total of 33 normal modes of vibration. The vibrational representation of those optical phonon modes at the center of the Brillouin zone can be given by equation 3C.1.

$$\Gamma = 4B_{1u} + 3B_{2u} + 4B_{3u} + 4A_g + 5B_{1g} + 4B_{2g} + 5B_{3g} + 4A_u \quad \dots\dots (3C.1)$$

All these nondegenerate vibrational modes are infrared-active ( $B_{1u}$ ,  $B_{2u}$ , and  $B_{3u}$ ), Raman-active ( $A_g$ ,  $B_{1g}$ ,  $B_{2g}$ , and  $B_{3g}$ ), and the  $A_u$  modes are silent. The vibrational modes on the spectrum do not match with characteristic modes of tetragonal (rutile) and deformed rutile phase of SnO<sub>2</sub>, which is in well agreement with the XRD results. However, till date no spectral analysis for Raman spectrum of SnO<sub>2</sub> in its orthorhombic (scrutinyite) phase has been reported yet. As there is scarce of data in the literature, therefore it is difficult to completely assign the observed phonon modes. Hence, we can confirm the formation of orthorhombic phase of SnO<sub>2</sub> in resemblance with Raman



spectrum of the  $\alpha$ -PbO<sub>2</sub> (scrutinyite) and metal oxides having scrutinyite crystal structure [70-72].



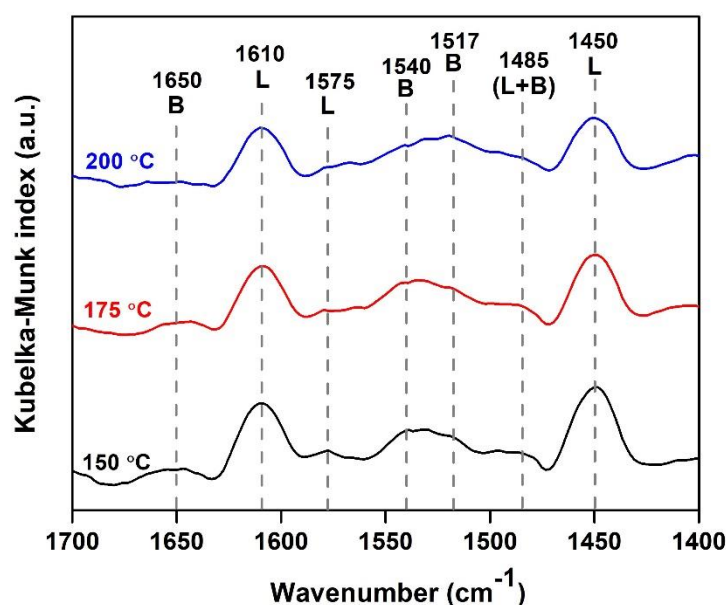
**Figure 3C.4** XPS spectrum of Sn 3d (a) and O 1s (b), BET isotherm (c) and pore size distribution (d) of the scrutinyite-SnO<sub>2</sub> NS assembly.

The XPS analysis is performed to investigate the chemical state of the SnO<sub>2</sub> NSs (Figure 3C.4(a, b)). The Sn 3d XPS spectrum displays two peaks at binding energy 486.1 and 494.5 eV for Sn 3d<sub>5/2</sub> and 3d<sub>3/2</sub> state, respectively (Figure 4a). The binding energies of are very close to the standard data for Sn<sup>4+</sup> and no peaks either for Sn<sup>2+</sup> or Sn<sup>0</sup> is detected. The energy difference of 8.4 eV between Sn 3d<sub>5/2</sub> and Sn 3d<sub>3/2</sub> state is in accordance with reported value of energy splitting for Sn(IV)O<sub>2</sub>. Again, in the O 1s spectrum two deconvoluted peaks located at binding energy 530.1 and 531.5 eV is observed (Figure 4b). The peak at 530.1 eV is ascribed to oxygen bound to Sn in the SnO<sub>2</sub> crystal lattice. Another peak located at 531.5 eV is attributed to adsorbed oxygen (O<sup>-</sup> and O<sup>2-</sup>) species (e.g., OH and H<sub>2</sub>O), respectively. Finally, the XPS spectra indicate that the synthesized nanosheets are Sn(IV)O<sub>2</sub> rather than Sn(II)O or Sn(0) metals [68, 73, 74].

The nitrogen adsorption–desorption analysis is also carried out to determine the specific surface area and pore size of the as-synthesized SnO<sub>2</sub> NS assembly. A type IV isotherm characteristic of mesoporous material with hysteresis loop H3-type according to IUPAC is observed for the sample (Figure 3C.4c). The BET surface area about to 71.7

$\text{m}^2\text{g}^{-1}$  is found for the NSs, which is comparatively larger than the surface area of commercial  $\text{SnO}_2$  powder (Sigma-Aldrich;  $38.3 \text{ m}^2\text{g}^{-1}$ ) and quite reasonable for  $\text{SnO}_2$  nanomaterial [73, 74]. Again, the pore size distribution based on the BJH model is determined from the desorption branch of the isotherm. The BJH pore volume and diameter  $0.21 \text{ cm}^3\text{g}^{-1}$  and  $3.99 \text{ nm}$ , respectively is observed for the sample. The maximum of pore size distribution from the curve is observed at  $3.99 \text{ nm}$  clearly indicating the mesoporosity of the sample (Figure 3C.4d).

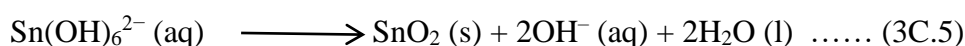
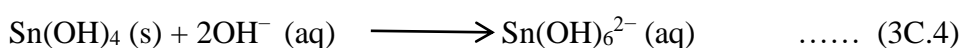
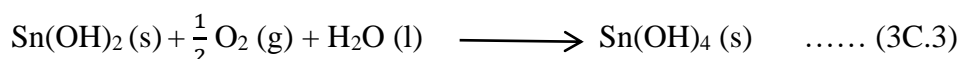
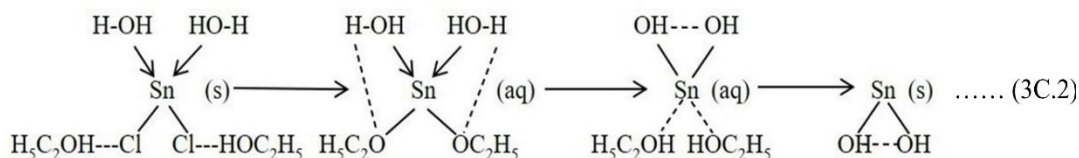
To evaluate the acidity of the synthesized  $\text{SnO}_2$  NSs, the temperature programmed desorption of ammonia ( $\text{NH}_3$ -TPD) is performed (Figure A.4 of Appendix). The  $\text{NH}_3$ -TPD profile shows a broad desorption peak in the range  $250$ – $550 \text{ }^\circ\text{C}$ . In general, strength of acidic sites can be divided into weak ( $200$ – $300 \text{ }^\circ\text{C}$ ), medium ( $300$ – $450 \text{ }^\circ\text{C}$ ) and high ( $> 450 \text{ }^\circ\text{C}$ ) regions [75, 76]. The measured  $\text{NH}_3$ -TPD profile is deconvoluted into three peaks having maximal temperatures at  $\sim 320 \text{ }^\circ\text{C}$ ,  $361 \text{ }^\circ\text{C}$  and  $446 \text{ }^\circ\text{C}$  corresponding to 23%, 45% and 32%, respectively of the total desorbed amount of  $\text{NH}_3$ . All the peaks can be assigned to the medium temperature region ( $300$ – $450 \text{ }^\circ\text{C}$ ), which indicates the presence of medium strength acidic sites in the  $\text{SnO}_2$  nanosheets [77]. Moreover, the nature and stability of the acidic sites in the synthesized  $\text{SnO}_2$  NSs are evaluated by performing Py-FTIR analysis at different temperatures and the results are presented in Figure 3C.5. The Py-FTIR spectra exhibit bands at  $1610$ ,  $1575$  and



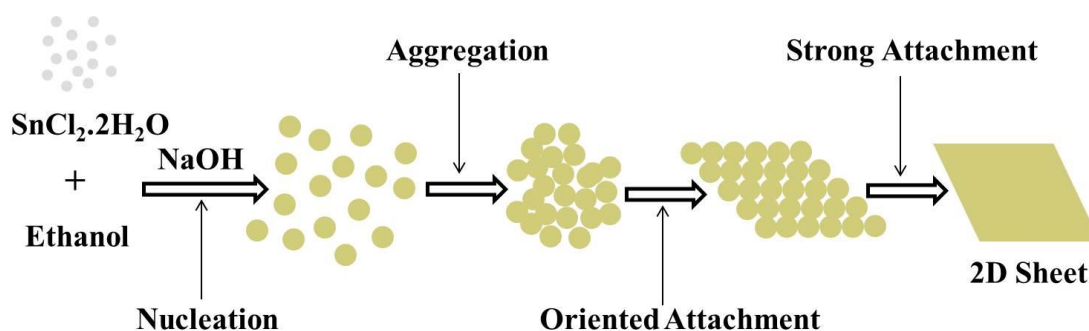
**Figure 3C.5** Py-FTIR spectra of synthesized  $\text{SnO}_2$  nanosheets assembly at different temperatures.

1450  $\text{cm}^{-1}$  corresponding to vibrational modes of pyridine coordinated at Lewis acidic sites (L). The bands at 1610 and 1450  $\text{cm}^{-1}$  correspond to pyridine bound to strong Lewis acidic sites, whereas the band at 1575  $\text{cm}^{-1}$  corresponds to pyridine bound to weak Lewis acidic sites [78]. Again, pyridine molecules protonated at Brönsted acidic sites (B) are responsible for the bands at 1650, 1540 and 1517  $\text{cm}^{-1}$  [79, 80]. Furthermore, another weak band at 1485  $\text{cm}^{-1}$  is caused by pyridine which is linked to both Lewis and Brönsted acidic sites (L+B) [81]. All the bands continue to be thermally stable at 200 °C, suggesting that the acidic sites of the nanosheets remain intact.

By following the experimental results, we can propose a reasonable mechanism for the formation of 2D  $\text{SnO}_2$  nanosheets. The 2D  $\text{SnO}_2$  NSs can be obtained by the solvothermal treatment of Sn(II) salts in alkaline aqueous solution in presence of ethanol via hydrolysis, oxidation and decomposition of Sn(II) salts/ions [70-72, 82, 83]. In general, the hydrolysis of Sn(II) salt may lead to formation of layered/sheet-like hydroxide intermediates, which further oxidize and/or decompose to sheet-like structure of  $\text{SnO}_2$  [73, 74]. Therefore, chemical reactions involved during the synthesis process can be described as follows:



As the solution is rich in ethanol, initially  $\text{Cl}^-$  is replaced from  $\text{SnCl}_2 \cdot 2\text{H}_2\text{O}$  molecule by the  $\text{C}_2\text{H}_5\text{OH}$  (equation 3C.2). Later, the  $\text{H}_2\text{O}$  molecules may attack the  $\text{Sn-OC}_2\text{H}_5$  bonds and replace the  $\text{C}_2\text{H}_5\text{OH}$  molecules to form  $\text{Sn(OH)}_2$  (equation 3C.2). Subsequently, the  $\text{Sn(OH)}_2$  may undergo oxidation to the precipitate as  $\text{Sn(OH)}_4$  (equation 3C.3). Afterward, the  $\text{OH}^-$  ion from the alkaline ( $\text{NaOH}$ ) solution interacts with  $\text{Sn(OH)}_4$  and forms  $\text{Sn(OH)}_6^{2-}$  (equation 3C.4). Further, decomposition of  $\text{Sn(OH)}_6^{2-}$  may take place forming the crystals of  $\text{SnO}_2$  (equation 3C.5). Finally, the formation and self-construction mechanism of 2D  $\text{SnO}_2$  NSs by oriented attachment from 0D nanocrystallites is schematically represented in Scheme 3C.1.



**Scheme 3C.1** Schematic representation of formation and self-construction mechanism of 2D SnO<sub>2</sub> nanosheet ( $l \approx 140$  nm,  $b \approx 85$  nm and  $h \approx 1.32$  nm).

### 3C.1.2 Catalytic activity of SnO<sub>2</sub> nanosheets under conventional condition

The FC acylation reaction over as-synthesized single crystalline and ultrathin SnO<sub>2</sub> NS assembly is carried out to evaluate its catalytic activity. To determine the standard experimental conditions, we have chosen the acylation reaction of anisole (aromatic substrate) and benzoyl chloride (acylating agent) as a model reaction. No product formation takes place without the catalyst in the reaction suggesting the role of the catalyst (Table 3C.1, entry 1). As the temperature has a significant role on a reaction therefore at first, we have tested the reaction at different temperatures and observed that the yield of product 4-methoxybenzophenone (3a) is considerably affected by reaction temperature (Figure A.5 of Appendix). The increase in reaction temperature from room temperature (= 27 °C) to 50 °C enhanced the yield of product from 46 to 92%, respectively perhaps due to the higher molecular thermal agitation and collision probability between the benzoyl cation and the arene [84]. Further increase in the reaction temperature does not alter the yield of aromatic ketone. Thus, the reaction temperature 50 °C is considered as a prime temperature for the major yield of aromatic ketones in presence of as-synthesized SnO<sub>2</sub> NSs.

To achieve maximum yield of product, the reaction is optimized by changing the amount of catalyst (Figure A.6 of Appendix). The figure shows that as the amount of catalyst increases the yield of the product of the reaction increases due to increase in concentration of benzoyl cation that accelerates the reaction and a maximum yield of the product is observed with 10 mol % of catalyst [84]. No further improvement of reaction yield is observed on employing more than 10 mol % SnO<sub>2</sub> nanocatalyst, presumably due to the fact that the reaction mixture becomes more viscous leading to resistance in mass

transfer. The observations suggest that a notable result is obtained when the acylation reaction is carried out with 10 mol % of SnO<sub>2</sub> nanocatalyst at 50 °C.

Moreover, the effect of solvent on the entitled reaction is observed in the presence of five different solvents (Table 3C.1). Though the reaction progress is smooth in the presence of solvents, miserable yields of the product are observed (Table 3C.1, entries 2–6). Trace amount of product is detected with solvents ethyl acetate and tetrahydrofuran having strong coordination ability (Table 3C.1, entries 4 and 5) [85]. The same reaction if carried out in nitromethane or acetonitrile, only 45 and 46% yields is detected, respectively. Noticeably, dichloromethane provides a better amount of product yet a less improvement (59% yield) is noticed (Table 3C.1, entry 6). Meanwhile, the acylation of anisole is also performed under solvent-free conditions, resulting in a commendable yield of 92% (Table 3C.1, entry 7). The observation suggests that there is no significant effect of solvents in the reaction, in agreement with literature reports and a good result is obtained by employing the aromatic ether as the self-solvent [86].

**Table 3C.1** Effect of solvent on the acylation of anisole with benzoyl chloride<sup>a</sup>

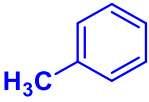

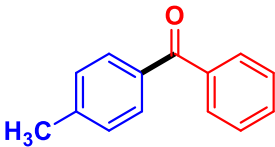
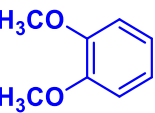
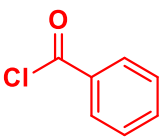
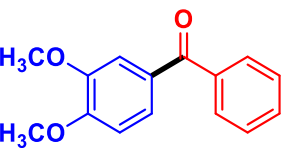
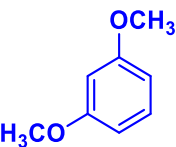
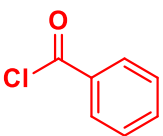
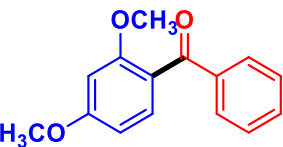
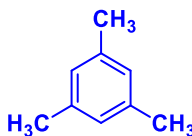
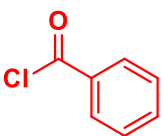
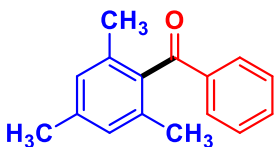
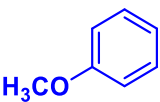
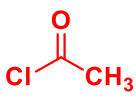
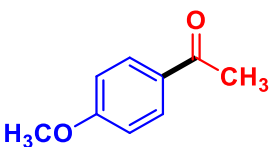
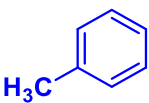
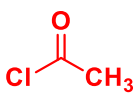
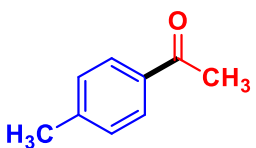
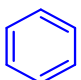
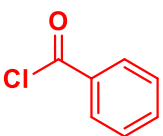
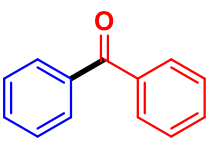
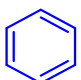
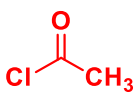
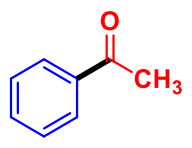
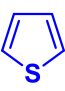
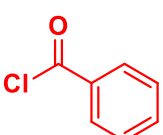
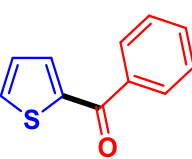
Entry	Catalyst	Solvent	Time (min)	Yield <sup>b</sup> (%)
1	None	Solvent free	>120	0
2	SnO <sub>2</sub>	Acetonitrile	120	46
3	SnO <sub>2</sub>	Nitromethane	120	45
4	SnO <sub>2</sub>	Ethyl Acetate	120	Trace
5	SnO <sub>2</sub>	Tetrahydrofuran	120	Trace
6	SnO <sub>2</sub>	Dichloromethane	120	59
7	SnO <sub>2</sub>	Solvent free	50	92

<sup>a</sup>Reaction Conditions: anisole (4 mmol), benzoyl chloride (2 mmol), solvent (0.5 mL), catalyst (10 mol%) and temperature (50 °C).

<sup>b</sup>Isolated yield.

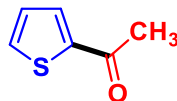
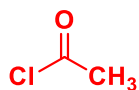
To explore the substrate scope of the reaction, a range of aromatic compounds and acid chlorides are reacted under optimized conditions and the subsequent results are presented in Table 3C.2. It is observed that the acylation happens exclusively at the position para to methoxy (–OCH<sub>3</sub>) and methyl (–CH<sub>3</sub>) groups for all the substituted aromatic compounds furnishing corresponding products within 40–70 min (Table 3C.2, entries 1–6). The presence of electron releasing –OCH<sub>3</sub> and –CH<sub>3</sub> groups in these cases

**Table 3C.2** Substrate scope for Friedel-Crafts acylation reaction over SnO<sub>2</sub> nanosheets<sup>a</sup>

Entry	Substrate	Acid chloride	Product	Time (min)	Yield <sup>b</sup> (%)
1				70	84
2				60	86
3				50	80
4				40	78
5				50	87
6				60	83
7				>120	Trace
8				120	40
9				50	86



10



40

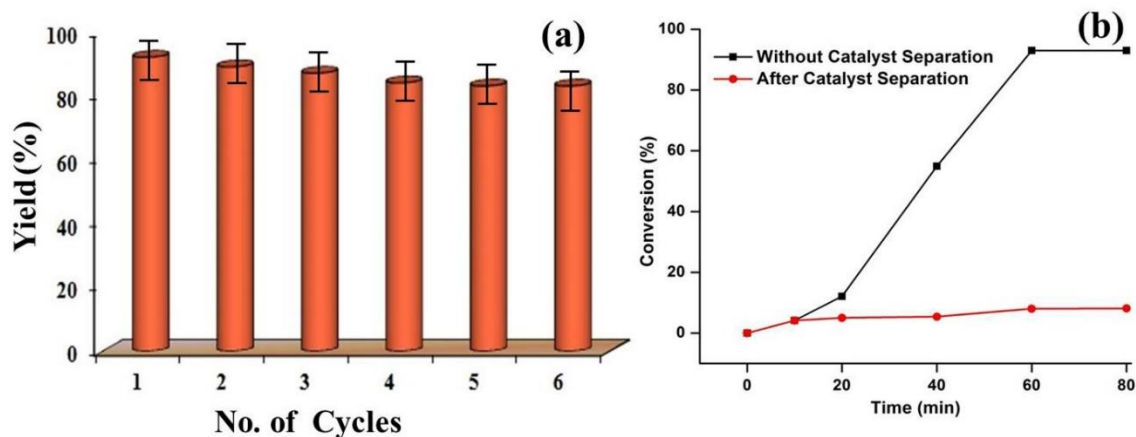
84

<sup>a</sup>Reaction Conditions: substrate (4 mmol), acid chloride (2 mmol), catalyst (10 mol%) and temperature (50 °C).

<sup>b</sup>Isolated yield.

resulted in good to high yields (78–92%) of corresponding aromatic ketones at 50 °C. However, the acylation of benzene (Table 3C.2, entries 7 and 8) proceeds after vigorous stirring affording low yields of corresponding product due to its low activity [87]. The reaction proceeds well with five membered heterocyclic compounds such as thiophene (Table 3C.2, entries 9 and 10), yielding quantitative amounts of 2-acylated products. The SnO<sub>2</sub> NS assembly exhibits remarkable activity with excellent regioselectivity under solvent free reaction condition, which may be attributed to ultrathin two-dimensional (2D) confinement effect, acid site and the redox behavior of the SnO<sub>2</sub> nanosheets.

Recyclability of catalyst is a prime factor regarding environmental sustainability and economic industrial processes. For checking the recyclability of the catalyst, six repeated cycles of catalytic reaction are performed and presented in Figure 3C.6a. The high yield of aromatic ketone is retained without significant loss of activity up to sixth consecutive run, indicating the fair stability of the catalyst. The minute decrease in activity may be considered for the unavoidable mechanical loss of catalyst during separation from every previous runs. Moreover, a hot filtration test is conducted to investigate the leaching of the SnO<sub>2</sub> nanocatalyst (Figure 3C.6b). After the first 10 min expedition of the model reaction between anisole and benzoyl chloride under optimized conditions, the catalyst is separated from the mixture by simple filtration. The filtrated reaction mixture is further continued for additional 50 min. No obvious enhancement of the % conversion is noticed after separation of the catalyst suggesting no significant leaching of the catalyst. After completion of sixth run, the composition and morphology of the recovered SnO<sub>2</sub> nanocatalyst is studied by using FTIR, XRD and TEM/HRTEM analyses. The FTIR spectrum of the recycled catalyst exhibited no significant changes, implying that the functionalities of the catalyst remained unchanged even after six consecutive runs (Figure A.7 of Appendix). Powder XRD pattern of the reused catalyst

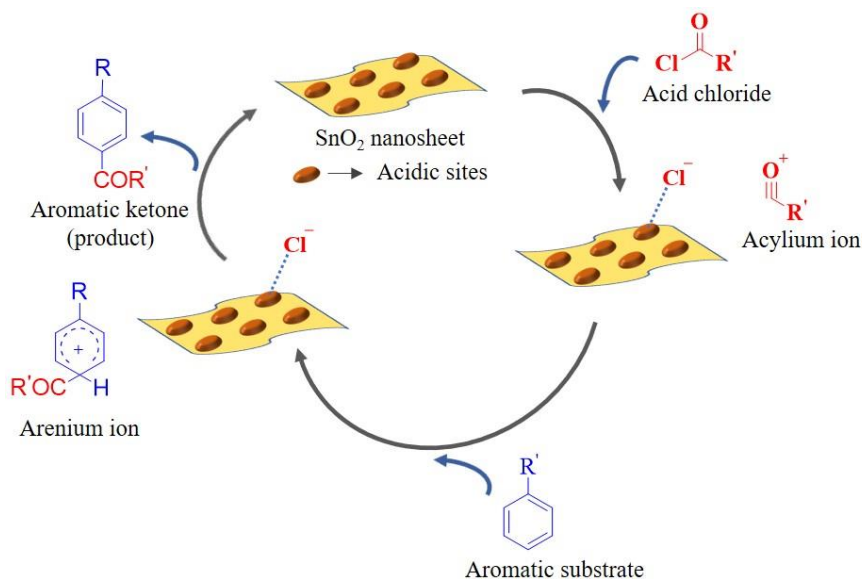


**Figure 3C.6.** Recyclability test (a) and hot filtration test for leaching (b) of the SnO<sub>2</sub> nanocatalyst.

also shows inconsequential changes than that of the fresh catalyst confirming the good structural stability of the catalyst (Figure A.8a of Appendix). TEM investigation of the reused catalyst reveals that the nanosheets of the SnO<sub>2</sub> catalyst are very slightly broken and stacked compared to those of the fresh catalyst probably due to continuous stirring under heat (A.8b of Appendix). However, the distinctly visible lattice fringes in the HRTEM images indicate that the crystallinity of the nanosheets is still intact in the recovered catalyst (inset in A.8b of Appendix). The overall TEM observation confirms the high structural and morphological stability of the catalyst.

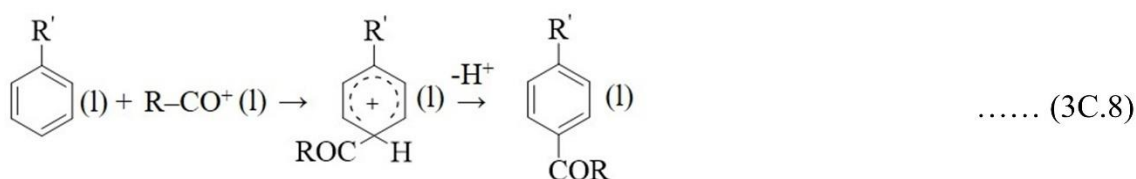
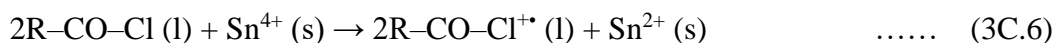
### 3C.1.3 Proposed reaction mechanism for the FC acylation over SnO<sub>2</sub> nanosheets

The plausible mechanism involved for the action of SnO<sub>2</sub> NSs in acid catalyzed Friedel-Crafts acylation is shown in Scheme 3C.2. FC acylation is an electrophilic aromatic substitution reaction, and the reaction is due to the generation of an acyl carbonium ion. Mainly, acidic sites of the nanocatalyst facilitate formation of the acylium ion. At first, adsorption of the acid chloride occurs place on the acidic site of the SnO<sub>2</sub> nanocatalyst that converts into acylium ion. This acylium ion acts as an electrophile and reacts with nucleophilic aromatic substrate to generate corresponding aromatic ketone.



**Scheme 3C.2** Schematic representation of acid catalyzed mechanism of Friedel-Crafts acylation over SnO<sub>2</sub> nanosheet ( $l \approx 140$  nm,  $b \approx 85$  nm and  $h \approx 1.32$  nm).

Again, the reduction of Sn<sup>4+</sup> to Sn<sup>2+</sup> is relatively easy owing to the positive standard reduction potential for Sn<sup>4+</sup> (aq) + 2e<sup>-</sup> → Sn<sup>2+</sup> (aq) ( $E^{\circ}_{\text{Sn}^{4+}/\text{Sn}^{2+}} = +0.13$  V) [88]. Therefore, along with the conventional acid catalyzed mechanism for FC acylation, a redox mechanism also can be expected [89, 90]. The steps involved in this pathway are mentioned below:



The acid chloride gets activated to 2R-CO-Cl<sup>\*·</sup> with the reduction of Sn<sup>4+</sup> to Sn<sup>2+</sup> simultaneously (equation 3C.6), thereby generating the R-CO<sup>+</sup> carbocation (equation 3C.7). Subsequently, the carbocation reacts with the aromatic substrate resulting in the formation of acylated product (equation 3C.8). Further, Sn<sup>2+</sup> is oxidized back to Sn<sup>4+</sup> (equation 3C.9) followed by liberation of HCl (equation 3C.10).

Finally, we compared some results obtained in this work with that of other metal oxide catalysts and the outcomes are listed in Table 3C.3. In case of  $ZrO_2$ ,  $Fe_2O_3$  and  $Fe_2O_3/HY$  (Table 3C.3, entries 1–3), although the reaction is performed in solvent less condition, it required prolonged time to furnish the products with comparatively lower yields than the present protocol. Though the results obtained with PANI/nano-ZnO and  $SnO_2-SiO_2$  (Table 3C.3, entries 4 and 5) are comparable to that of the present protocol, these methods require the preparation of catalyst support.

**Table 3C.3** Comparative study for FC acylation of aromatic compounds with benzoyl chloride using different metal oxide catalysts.

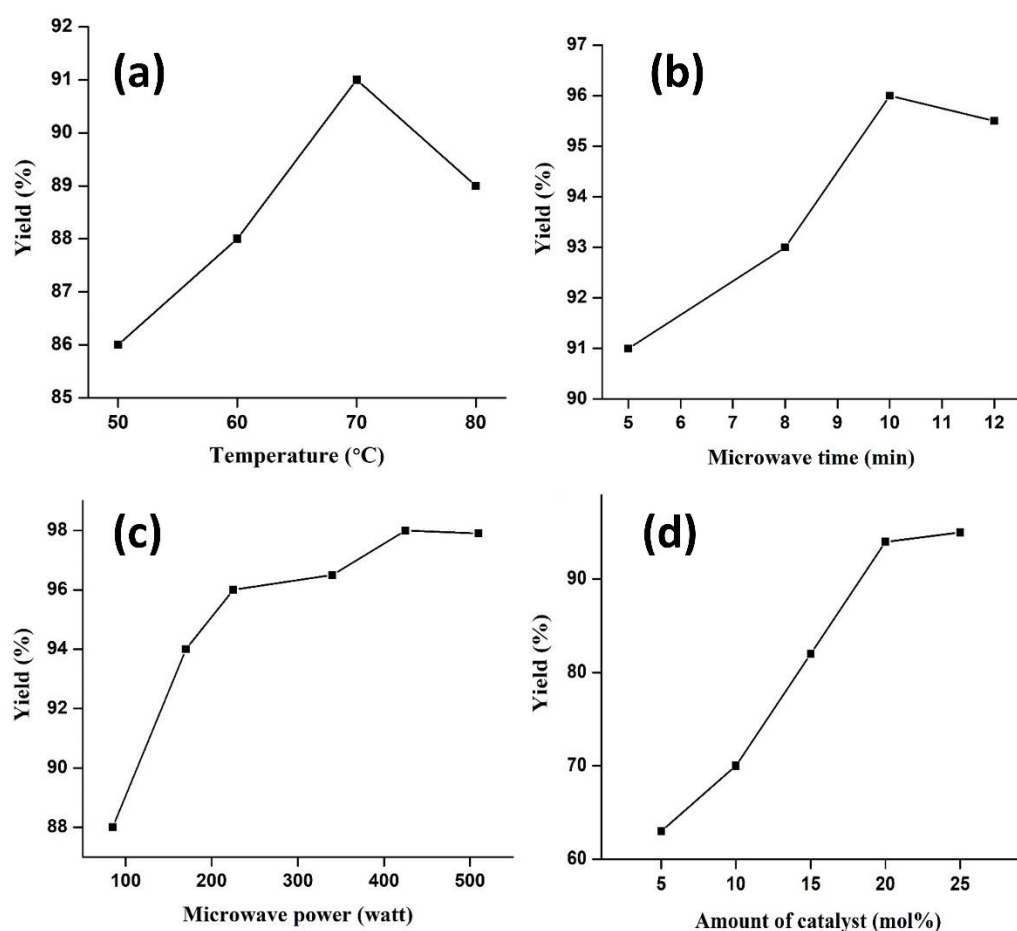
Entry	Catalyst	Substrate	Condition	Time	Yield (%)	Refs
1	$ZrO_2$	Anisole	Solvent free/120 °C	5 h	65	91
2	$Fe_2O_3$	Anisole	Solvent free/80 °C	120 min	32	92
3	$Fe_2O_3/HY$	Toluene	Solvent free/110 °C	10 h	43	93
4	PANI/nano-ZnO	Anisole	Solvent free/rt	10 min	95	94
5	$SnO_2-SiO_2$	Anisole	$CH_3NO_2/80$ °C	30 min	86	95
6	$TiO_2$	Toluene	Solvent free/80 °C/MW	20 sec	68	96
7	$SnO_2$ NSs	Anisole	Solvent free/50 °C	50 min	92	this work
8	$SnO_2$ NSs	Toluene	Solvent free/50 °C	60 min	84	this work

The FC acylation of toluene with  $TiO_2$  (Table 3C.3, entry 6) completes quickly within 20 second. However, it requires higher reaction temperature (80 °C) and yields lower amount (68%) of corresponding product. These results clearly disclose that the synthesized  $SnO_2$  nanosheets can be well utilized as an alternative for the regioselective acylation of aromatic compounds.

#### 3C.1.4 Catalytic activity of $SnO_2$ nanosheets under microwave irradiation condition

The core heating mechanism in microwave (MW) irradiation technology facilitates the activation of reactant molecules yielding desired products in short time period [97]. Therefore, combination of the advantages of MW irradiation with solid acid catalytic system helps in attaining high yield in short reaction time. The catalytic activity of the  $SnO_2$  NS assembly is evaluated for Friedel-Crafts acylation reaction under MW irradiation conditions. To identify the optimum reaction conditions for attaining notable

yields of corresponding aromatic ketone product, the effect of MW temperature, MW power, time, and amount of SnO<sub>2</sub> NSs are explored. The influence of MW temperature on benzylation of anisole is shown in Figure 3C.7a. It can be observed that, as the temperature is increased, yield of 4-methoxybenzophenone (**3c**) increases rapidly to a peak value at 70 °C, probably due to the increasing molecular movement and collision probability between the benzoyl cation and the arene. However, increasing the reaction temperature to 80 °C did not result in improvement of product yield. These results suggest that 70 °C is the optimum reaction temperature for the synthesized SnO<sub>2</sub> NSs.



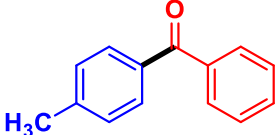
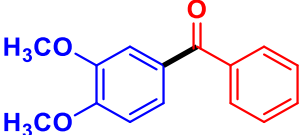
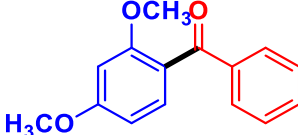
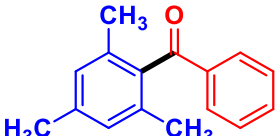
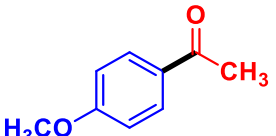
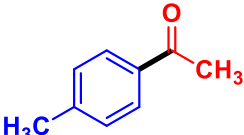
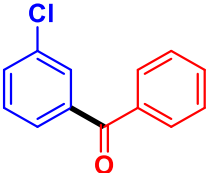
**Figure 3C.7** Optimization of reaction conditions: temperature (a), microwave time (b), microwave power (c), and amount of catalyst (d). Reaction conditions: anisole (4 mmol) and benzoyl chloride (2 mmol).

In general, prolonged reaction time favours the productivity of a reaction. The variation in yield of product with respect to MW time is presented in Figure 3C.7b. As expected, a pronounced enhancement of the yield of **3c** is observed as the MW time is increased, yielding a maximum value of 96% in 10 min. Hence, 10 min is chosen as the

optimum microwave time for SnO<sub>2</sub> NSs catalyzed synthesis of 4-methoxybenzophenone. Likewise, the effect of MW power on the reaction is scrutinized and the results are depicted in Figure 3C.7c. The yield grew dramatically to a peak value at 425 watt, which can be attributed to the increased heating rate with increase in MW power. However, increasing the MW power to 510 watt had no effect on the yield of 4-methoxybenzophenone.

Again, the product yield enhances substantially with increasing the catalyst amount, owing to the increase in the number of acidic sites for interaction, reaching maximum yield at 25 mol% of catalyst loading (Figure 3C.7d). Considering all the observations together, a good result is achieved when the benzoylation reaction is carried out with 25 mol% of SnO<sub>2</sub> NSs with a microwave power of 425 watt for 10 min at 70 °C.

**Table 3C.4** Study of substrate scope for FC acylation reaction under microwave irradiation<sup>a</sup>

		
<b>a</b>	<b>b</b>	<b>c</b>
20 min, 92%	10 min, 93%	10 min, 92%
		
<b>d</b>	<b>e</b>	
20 min, 86%	10 min, 95%	
		
<b>f</b>	<b>g</b>	
20 min, 92%	>20 min, n.r	

<sup>a</sup>Reaction conditions: arene (4 mmol), acid chloride (2 mmol), ZO-15 (25 mol%), MW power = 425 watt and temperature = 70 °C



The generality and versatility of this method is investigated by expanding the study to a variety of arenes under optimized reaction conditions. The reaction of aromatic substrates with electron-releasing groups, such as  $-\text{OCH}_3$  and  $-\text{CH}_3$  afforded 86 to 95% yield of the corresponding para-substituted aromatic ketones (Table 3C.4, entries a–f). However, acylation of chlorobenzene is sluggish and the conversion is negligible due to the electron withdrawing property of  $-\text{Cl}$  group which deactivates the benzene ring for acylation (Table 3C.4, entry g). It is observed that the reaction proceeds faster in comparison to room temperature methodology described in the previous section and gives respectable yields (86-95%) within 10 to 20 min.

In summary, a facile and robust solvothermal route has been reported for the synthesis of single crystalline and ultrathin nanosheet assembly of  $\text{SnO}_2$ . The structural analyses have revealed that the  $\text{SnO}_2$  NSs are ultrathin and single crystallized in the scrutinyite- $\text{SnO}_2$  phase with high purity. The ultrathin  $\text{SnO}_2$  NSs have exposed preferential growth in the [011] direction on the main surface with a thickness of *ca.* 1.3 nm. Furthermore, the  $\text{SnO}_2$  NSs are tested for the regioselective FC acylation to synthesize aromatic ketones in solvent-free reaction conditions. The acylation reaction over the  $\text{SnO}_2$  NSs afforded predominantly para-substituted ketones with yields up to 92% under mild reaction conditions. The catalytic study is also extended to microwave irradiated FC acylation and commendable yields are obtained in shorter reaction times. The comprehensive catalytic study has shown that the  $\text{SnO}_2$  NS assembly is a superior catalytic material in comparison to other metal oxide catalysts used so far with respect to its activity and reproducibility.

**REFERENCES**

- [1] Sartori, G. and Maggi, R. Use of solid catalysts in Friedel-Crafts acylation reactions. *Chemical Reviews*, 106(3):1077–1104, 2006.
- [2] Pandey, G., Tiwari, S. K., Singh, B., Vanka, K., and Jain, S. *p*-Selective (sp<sup>2</sup>)-C–H functionalization for an acylation/alkylation reaction using organic photoredox catalysis. *Chemical Communications*, 53(91):12337–12340, 2017.
- [3] Olah, G. A. *Friedel-Crafts Chemistry*. Wiley: New York, 1973.
- [4] Jin, X., Wang, A., Cao, H., Zhang, S., Wang, L., Zheng, X., and Zheng, X. A new efficient method for the preparation of intermediate aromatic ketones by Friedel-Crafts acylation. *Research in Chemical Intermediates*, 44(9):5521–5530, 2018.
- [5] Zuidema, D. R., Williams, S. L., Wert, K. J., Bosma, K. J., Smith, A. L., and Mebane, R. C. Deoxygenation of aromatic ketones using transfer hydrogenolysis with raney nickel in 2-propanol. *Synthetic Communications*, 41(19):2927–2931, 2011.
- [6] Mu, M., Fang, W., Liu, Y., and Chen, L. Iron(III)-modified tungstophosphoric acid supported on titania catalyst: Synthesis, characterization, and Friedel-Craft acylation of *m*-xylene. *Industrial & Engineering Chemistry Research*, 54(36):8893–8899, 2015.
- [7] Wang, J., Pang, Y.-B., Tao, N., Zeng, R., and Zhao, Y. Nickel-catalyzed, *para*-selective, radical-based alkylation of aromatic ketones. *Organic Letters*, 22(3):854–857, 2020.
- [8] Zhao, J., Hughes, C.O., and Toste, F. D. Synthesis of aromatic ketones by a transition metal-catalyzed tandem sequence. *Journal of the American Chemical Society*, 128(23):7436–7437, 2006.
- [9] Kusumaningsih, T., Prasetyo, W. E., and Firdaus, M. A greatly improved procedure for the synthesis of an antibiotic-drug candidate 2,4-diacetylphloroglucinol over silica sulphuric acid catalyst: Multivariate optimisation and environmental assessment protocol comparison by metrics. *RSC Advances*, 10(53):31824–31837, 2020.
- [10] Sawant, R. T., Stevens, M. Y., and Odell, L. R. Microwave-assisted *aza*-friedel-crafts arylation of *n*-acyliminium ions: Expedient access to 4-aryl 3,4-dihydroquinazolinones. *ACS Omega*, 3(10):14258–14265, 2018.
- [11] Schlegel, M. and Schneider, C. Lewis acid-catalyzed Friedel-Crafts reactions

- toward highly versatile,  $\alpha$ -quaternary oxime ethers. *Chemical Communications*, 54(79):11124–11127, 2018.
- [12] Firouzabadi, H., Iranpoor, N., and Nowrouzi, F. Solvent-free Friedel-Crafts acylation of aromatic compounds with carboxylic acids in the presence of trifluoroacetic anhydride and aluminum dodecatungstophosphate. *Tetrahedron Letters*, 44 (28), 5343–5345, 2003.
- [13] Kawada, A., Mitamura, S., and Kobayashi, S.  $\text{Ln}(\text{OTf})_3\text{-LiClO}_4$  as reusable catalyst system for Friedel-Crafts acylation. *Chemical Communications*, 02(2):183–184, 1996.
- [14] Bartoli, G., Bosco, M., Marcantoni, E., Massaccesi, M., Rinaldi, S., and Sambri, L.  $\text{LiClO}_4$ -acyl anhydrides complexes as powerful acylating reagents of aromatic compounds in solvent free conditions. *Tetrahedron Letters*, 43(36):6331–6333, 2002.
- [15] Fürstner, A., Voigtländer, D., Schrader, W., Giebel, D., and Reetz, M. T. A “hard/soft” mismatch enables catalytic Friedel-Crafts acylations. *Organic Letters*, 3(3):417–420, 2001.
- [16] Kusama, H. and Narasaka, K. Friedel-Crafts acylation of arenes catalyzed by bromopentacarbonylrhenium(I). *Bulletin of the Chemical Society of Japan*, 68(8):2379–2383, 1995.
- [17] Doan, T. L. H., Dao, T. Q., Tran, H. N., Tran, P. H., and Le, T. N. An efficient combination of Zr-MOF and microwave irradiation in catalytic lewis acid Friedel-Crafts benzylation. *Dalton Transactions*, 45(18):7875–7880, 2016.
- [18] Motiwala, H. F., Vekariya, R. H., and Aubé, J. Intramolecular Friedel-Crafts acylation reaction promoted by 1,1,1,3,3,3-hexafluoro-2-propanol. *Organic Letters*, 17 (21), 5484–5487, 2015.
- [19] Reddy, B. M. and Patil, M. K. Organic syntheses and transformations catalyzed by sulfated zirconia. *Chemical Reviews*, 109(6):2185–2208, 2009.
- [20] Tran, P. H., Nguyen, T. D. T., Tu, T. A. T., and Le, T. N. Magnetically recoverable  $\gamma\text{-Fe}_2\text{O}_3$  nanoparticles as a highly active catalyst for Friedel-Crafts benzylation reaction under ultrasound irradiation. *Arabian Journal of Chemistry*, 13 (1):290–297, 2020.
- [21] Liu, E., Locke, A. J., Frost, R. L., and Martens, W. N. Sulfated fibrous  $\text{ZrO}_2/\text{Al}_2\text{O}_3$  core and shell nanocomposites: A novel strong acid catalyst with hierarchically

- macro-mesoporous nanostructure. *Journal of Molecular Catalysis A: Chemical*, 353–354:95–105, 2012.
- [22] Hua, W., Xia, Y., Yue, Y., and Gao, Z. Promoting effect of Al on  $\text{SO}_4^{2-}/\text{M}_x\text{O}_y$  (M= Zr, Ti, Fe) catalysts. *Journal of Catalysis*, 196(1):104–114, 2000.
- [23] Rao, X., Ishitani, H., Yoo, W., and Kobayashi, S. Zirconium- $\beta$  zeolite-catalyzed continuous-flow Friedel-Crafts acylation reaction. *Asian Journal of Organic Chemistry*, 8(3):316–319, 2019.
- [24] Cornélis, A., Gerstmans, A., Laszlo, P., Mathy, A., and Zieba, I. Friedel-Crafts acylations with modified clays as catalysts. *Catalysis Letters*, 6(1):103–109, 1990.
- [25] Sarvari, M. H. and Sharghi, H. Reactions on a solid surface. A simple, economical and efficient Friedel-Crafts acylation reaction over zinc oxide (ZnO) as a new catalyst. *The Journal of Organic Chemistry*, 69(20):6953–6956, 2004.
- [26] Yadav, G. D. and Yadav, A. R. Selectivity engineered Friedel-Crafts acylation of guaiacol with vinyl acetate to acetovanillone over cesium-modified heteropolyacid supported on K-10 clay. *Industrial & Engineering Chemistry Research*, 52(31):10627–10636, 2013.
- [27] Martínez, F., Morales, G., Martín, A., and van Grieken, R. Perfluorinated nafion-modified SBA-15 materials for catalytic acylation of anisole. *Applied Catalysis A: General*, 347(2):169–178, 2008.
- [28] Chavali, M. S. and Nikolova, M. P. Metal oxide nanoparticles and their applications in nanotechnology. *SN Applied Sciences*, 1(6):607, 2019.
- [29] Pla, D. and Gómez, M. Metal and metal oxide nanoparticles: A lever for C–H functionalization. *ACS Catalysis*, 6(6):3537–3552, 2016.
- [30] Gadipelly, C. and Mannepalli, L. K. Nano-metal oxides for organic transformations. *Current Opinion in Green and Sustainable Chemistry*, 15:20–26, 2019.
- [31] Lin, Z., Guo, F., Wang, C., Wang, X., Wang, K., and Qu, Y. Preparation and sensing properties of hierarchical 3D assembled porous ZnO from zinc hydroxide carbonate. *RSC Advances*, 4(10):5122–5129, 2014.
- [32] Wahab, R., Ansari, S. G., Kim, Y. S., Dar, M. A., and Shin, H. S. Synthesis and characterization of hydrozincite and its conversion into zinc oxide nanoparticles. *Journal of Alloys and Compounds*, 461(1-2):66–71, 2008.

- [33] Winiarski, J., Tylus, W., Winiarska, K., Szczygieł, I., and Szczygieł, B. XPS and FT-IR characterization of selected synthetic corrosion products of zinc expected in neutral environment containing chloride ions. *Journal of Spectroscopy*, 2018: 2079278, 2018.
- [34] Liang, J., Hu, Y., Wu, Y., and Chen, H. Fabrication and corrosion resistance of superhydrophobic hydroxide zinc carbonate film on aluminum substrates. *Journal of Nanomaterials*, 2013(1):139768, 2013.
- [35] Kakiuchi, K., Hosono, E., Kimura, T., Imai, H., and Fujihara, S. Fabrication of mesoporous ZnO nanosheets from precursor templates grown in aqueous solutions. *Journal of Sol-Gel Science and Technology*, 39(1):63–72, 2006.
- [36] Nassar, M.Y., Moustafa, M. M., and Taha, M. M. Hydrothermal tuning of the morphology and particle size of hydrozincite nanoparticles using different counterions to produce nanosized ZnO as an efficient adsorbent for textile dye removal. *RSC Advances*, 6(48):42180–42195, 2016.
- [37] Alhawi, T., Rehan, M., York, D., and Lai, X. Hydrothermal synthesis of zinc carbonate hydroxide nanoparticles. *Procedia Engineering*, 102:356–361, 2015.
- [38] Paino, I. M., J. Gonçalves, F., Souza, F. L., and Zucolotto, V. Zinc oxide flower-like nanostructures that exhibit enhanced toxicology effects in cancer cells. *ACS Applied Materials & Interfaces*, 8(48):32699–32705, 2016.
- [39] Fathima, A. F., Mani, R. J., Roshan, M. M., and Sakthipandi, K. Enhancing structural and optical properties of ZnO nanoparticles induced by the double co-doping of iron and cobalt. *Materials Today: Proceedings*, 49:2598–2601, 2022.
- [40] Alamdari, S., Sasani Ghamsari, M., Lee, C., Han, W., Park, H. H., Tafreshi, M. J., Afarideh, H., and Ara, M. H. M. Preparation and characterization of zinc oxide nanoparticles using leaf extract of *Sambucus ebulus*. *Applied Sciences*, 10(10):3620, 2020.
- [41] Fabbiyola, S., Kennedy, L. J., Aruldoss, U., Bououdina, M., Dakhel, A. A., and JudithVijaya, J. Synthesis of Co-doped ZnO nanoparticles via co-precipitation: Structural, optical and magnetic properties. *Powder Technology*, 286:757–765, 2015.
- [42] Šćepanović, M. G. B. M., Grujić-Brojčin, M., Vojisavljević, K., Bernik, S., and Srećković, T. Raman study of structural disorder in ZnO nanopowders. *Journal of Raman Spectroscopy*, 41(9):914–921, 2010.

- [43] Aljaafari, A., Ahmed, F., Awada, C., and Shaalan, N. M. Flower-like ZnO nanorods synthesized by microwave-assisted one-pot method for detecting reducing gases: Structural properties and sensing reversibility. *Frontiers in Chemistry*, 8:456, 2020.
- [44] Gavrilenko, E. A., Goncharova, D. A., Lapin, I. N., Nemoykina, A. L., Svetlichnyi, V. A., Aljulaih, A. A., Mintcheva, N., and Kulinich, S. A. Comparative study of physicochemical and antibacterial properties of ZnO nanoparticles prepared by laser ablation of Zn target in water and air. *Materials*, 12(1):186, 2019.
- [45] Baranowska-Korczyc, A., Kościński, M., Coy, E. L., Grześkowiak, B. F., Jasiurkowska-Delaporte, M., Peplińska, B., and Jurga, S. ZnS coating for enhanced environmental stability and improved properties of ZnO thin films. *RSC Advances*, 8(43):24411–24421, 2018.
- [46] Cuscó, R., Alarcón-Lladó, E., Ibanez, J., Artús, L., Jiménez, J., Wang, B., and Callahan, M. J. Temperature dependence of Raman scattering in ZnO. *Physical Review B*, 75(16):165202, 2007.
- [47] Claros, M., Setka, M., Jimenez, Y. P., and Vallejos, S. AACVD synthesis and characterization of iron and copper oxides modified ZnO structured films. *Nanomaterials*, 10(3):471, 2020.
- [48] Al-Gaashani, R., Radiman, S., Daud, A. R., Tabet, N., and Al-Douri, Y. J. C. I. XPS and optical studies of different morphologies of ZnO nanostructures prepared by microwave methods. *Ceramics International*, 39(3):2283–2292, 2013.
- [49] Zheng, J. H., Jiang, Q., and Lian, J. S., 2011. Synthesis and optical properties of flower-like ZnO nanorods by thermal evaporation method. *Applied Surface Science*, 257(11):5083–5087, 2011.
- [50] Singh, P., Simanjuntak, F. M., Wu, Y. C., Kumar, A., Zan, H. W., and Tseng, T. Y. Sensing performance of gas sensors fabricated from controllably grown ZnO-based nanorods on seed layers. *Journal of Materials Science*, 55(21):8850–8860, 2020.
- [51] Zhang, Q., Zhang, Y., Chen, J., and Liu, Q. Hierarchical structure kaolinite nanospheres with remarkably enhanced adsorption properties for methylene blue. *Nanoscale Research Letters*, 14(1):1–9, 2019.
- [52] Zhang, L., Zhao, J., Lu, H., Li, L., Zheng, J., Li, H., and Zhu, Z. Facile synthesis and ultrahigh ethanol response of hierarchically porous ZnO nanosheets. *Sensors and Actuators B: Chemical*, 161(1):209–215, 2012.



- [53] Guo, Y., Lin, S., Li, X., and Liu, Y. Amino acids assisted hydrothermal synthesis of hierarchically structured ZnO with enhanced photocatalytic activities. *Applied Surface Science*, 384:83–91, 2016.
- [54] Tanabe, K., Ishiya, C., Matsuzaki, I., Ichikawa, I., and Hattori, H. Acidic property and catalytic activity of TiO<sub>2</sub>·ZnO. *Bulletin of the Chemical Society of Japan*, 45(1):47–51, 1972.
- [55] Hu, S. H., Chen, Y. C., Hwang, C. C., Peng, C. H., and Gong, D. C. Analysis of growth parameters for hydrothermal synthesis of ZnO nanoparticles through a statistical experimental design method. *Journal of Materials Science*, 45(19):5309–5317, 2010.
- [56] Lin, Z., Guo, F., Wang, C., Wang, X., Wang, K., and Qu, Y. Preparation and sensing properties of hierarchical 3D assembled porous ZnO from zinc hydroxide carbonate. *RSC Advances*, 4(10):5122–5129, 2014.
- [57] Sutradhar, N., Sinhamahapatra, A., Pahari, S. K., Pal, P., Bajaj, H. C., Mukhopadhyay, I., and Panda, A. B. Controlled synthesis of different morphologies of MgO and their use as solid base catalysts. *The Journal of Physical Chemistry C*, 115(25):12308–12316, 2011.
- [58] Raula, M., Rashid, M. H., Paira, T. K., Dinda, E., and Mandal, T. K. Ascorbate-assisted growth of hierarchical ZnO nanostructures: sphere, spindle, and flower and their catalytic properties. *Langmuir*, 26(11):8769–8782, 2010.
- [59] Hoseini, S. J., Nasrabadi, H., Azizi, M., Beni, A. S., and Khalifeh, R. Fe<sub>3</sub>O<sub>4</sub> nanoparticles as an efficient and magnetically recoverable catalyst for Friedel–Crafts acylation reaction in solvent-free conditions. *Synthetic Communications*, 43(12):1683–1691, 2013.
- [60] Ahmad, T., Khatoun, S., and Coolahan, K. Structural, optical, and magnetic properties of nickel-doped tin dioxide nanoparticles by solvothermal method. *Journal of the American Ceramic Society*, 99(4):1207–1211, 2016.
- [61] Suthakaran, S., Dhanapandian, S., Krishnakumar, N., and Ponpandian, N. Hydrothermal synthesis of SnO<sub>2</sub> nanoparticles and its photocatalytic degradation of methylviolet and electrochemical performance. *Materials Research Express*, 6(8):0850i3, 2019.

- [62] Akhir, M. A. M., Mohamed, K., Lee, H. L., and Rezan, S. A. Synthesis of tin oxide nanostructures using hydrothermal method and optimization of its crystal size by using statistical design of experiment. *Procedia Chemistry*, 19:993–998, 2016.
- [63] Qiao, X., Yang, H., Chen, C., Lou, X., Sun, J., Chen, L., Fan, X., Zhang, L., and Shen, Q. Synthesis of monodispersed SnO<sub>2</sub> microspheres via solvothermal method. *Procedia Engineering*, 94:58–63, 2014.
- [64] Dai, S. and Yao, Z. Synthesis of flower-like SnO<sub>2</sub> single crystals and its enhanced photocatalytic activity. *Applied Surface Science*, 258(15):5703–5706, 2012.
- [65] Zayyoun, N., Jaber, B., Laanab, L., Ntsoenzok, E., and Bekkari, R. Effect of solvent on the morphological and optical properties of CuO nanoparticles prepared by simple sol-gel process. *Journal of Materials and Environmental Science*, 7(5):1791–1797, 2016.
- [66] Rashad, M. M., Ibrahim, I. A., Osama, I., and Shalan, A. E. Distinction between SnO<sub>2</sub> nanoparticles synthesized using co-precipitation and solvothermal methods for the photovoltaic efficiency of dye-sensitized solar cells. *Bulletin of Materials Science*, 37(4):903–909, 2014.
- [67] Adnan, R., Razana, N. A., Rahman, I. A., and Farrukh, M. A. Synthesis and characterization of high surface area tin oxide nanoparticles via the sol-gel method as a catalyst for the hydrogenation of styrene. *Journal of the Chinese Chemical Society*, 57(2):222–229, 2010.
- [68] Masuda, Y., Ohji, T., and Kato, K. Tin oxide nanosheet assembly for hydrophobic/hydrophilic coating and cancer sensing. *ACS Applied Materials & Interfaces*, 4(3):1666–1674, 2012.
- [69] Choi, P. G., Izu, N., Shirahata, N., and Masuda, Y. SnO<sub>2</sub> nanosheets for selective alkene gas sensing. *ACS Applied Nano Materials*, 2(4):1820–1827, 2019.
- [70] Wittkamper, J., Xu, Z., Kombaiyah, B., Ram, F., De Graef, M., Kitchin, J. R., Rohrer, G. S., and Salvador, P. A. Competitive growth of scrutinyite ( $\alpha$ -PbO<sub>2</sub>) and rutile polymorphs of SnO<sub>2</sub> on all orientations of columbite CoNb<sub>2</sub>O<sub>6</sub> substrates. *Crystal Growth & Design*, 17(7):3929–3939, 2017.
- [71] Bae, J., Park, J., Kim, H. Y., Kim, H., and Park, J. Facile route to the controlled synthesis of tetragonal and orthorhombic SnO<sub>2</sub> films by mist chemical vapor deposition. *ACS Applied Materials & Interfaces*, 7(22):12074–12079, 2015.

- [72] Carvalho, M. H., Pereira, E. C., and de Oliveira, A. J. A. Orthorhombic SnO<sub>2</sub> phase observed composite (Sn<sub>1-x</sub>Ce<sub>x</sub>)O<sub>2</sub> synthesized by sol-gel route. *RSC Advances*, 8(8):3958–3963, 2018.
- [73] Liu, Y., Jiao, Y., Zhang, Z., Qu, F., Umar, A., and Wu, X. Hierarchical SnO<sub>2</sub> nanostructures made of intermingled ultrathin nanosheets for environmental remediation, smart gas sensor, and supercapacitor applications. *ACS Applied Materials & Interfaces*, 6(3):2174–2184, 2014.
- [74] Xu, X., Zhuang, J., and Wang, X. SnO<sub>2</sub> quantum dots and quantum wires: Controllable synthesis, self-assembled 2D architectures, and gas-sensing properties. *Journal of the American Chemical Society*, 130(37):12527–12535, 2008.
- [75] Desai, D. S. and Yadav, G. D. Friedel-Crafts acylation of furan using chromium-exchanged dodecatungstophosphoric acid: Effect of support, mechanism and kinetic modelling. *Clean Technologies and Environmental Policy*, 23(8):2429–2441, 2021.
- [76] Pimerzin, A. A., Roganov, A. A., Verevkin, S. P., Konnova, M. E., Pilshchikov, V. A., and Pimerzin, A. A. Bifunctional catalysts with noble metals on composite Al<sub>2</sub>O<sub>3</sub>-SAPO-11 carrier and their comparison with CoMoS one in *n*-hexadecane hydroisomerization. *Catalysis Today*, 329:71–81, 2019.
- [77] Yang, X., Yasukawa, T., Yamashita, Y., and Kobayashi, S. Development of trifluoromethanesulfonic acid-immobilized nitrogen-doped carbon-incarcerated niobia nanoparticle catalysts for Friedel-Crafts acylation. *The Journal of Organic Chemistry*, 86(21):15800–15806, 2021.
- [78] Du, P., Zheng, P., Song, S., Wang, X., Zhang, M., Chi, K., Xu, C., Duan, A., and Zhao, Z. Synthesis of a novel micro/mesoporous composite material Beta-FDU-12 and its hydro-upgrading performance for FCC gasoline. *RSC Advances*, 6(2):1018–1026, 2016.
- [79] Maronna, M. M., Kruissink, E. C., Parton, R. F., Soulimani, F., Weckhuysen, B. M., and Hoelderich, W. F. Spectroscopic study on the active site of a SiO<sub>2</sub> supported niobia catalyst used for the gas-phase Beckmann rearrangement of cyclohexanone oxime to  $\epsilon$ -caprolactam. *Physical Chemistry Chemical Physics*, 18(32):22636–22646, 2016.

- [80] Mokaya, R. and Jones, W. Acidity and catalytic activity of aluminosilicate mesoporous molecular sieves prepared using primary amines. *Chemical Communications*, (8):983–985, 1996.
- [81] Kumari, P. K., Rao, B. S., Padmakar, D., Pasha, N., and Lingaiah, N. Lewis acidity induced heteropoly tungstate catalysts for the synthesis of 5-ethoxymethyl furfural from fructose and 5-hydroxymethylfurfural. *Molecular Catalysis*, 448:108–115, 2018.
- [82] Chen, Z., Lai, J. K. L., and Shek, C. H. Facile strategy and mechanism for orthorhombic SnO<sub>2</sub> thin films. *Applied Physics Letters*, 89(23):231902, 2006.
- [83] Li, X. and Qu, Y. Morphology evolution of tin-based oxide hierarchical structures synthesized by molten salt approach and their applications as anode for lithium ion battery. *Crystal Growth & Design*, 16(1):34–41, 2016.
- [84] Cai, M. and Wang, X. Activity of imidazolium-based ionic liquids as catalysts for Friedel-Crafts acylation of aromatic compounds. *Asian Journal of Chemistry*, 26(18):5981–5984, 2014.
- [85] Ghodke, S. V and Chudasama, U. V. Friedel-Crafts alkylation and acylation of aromatic compounds under solvent-free conditions using solid acid catalysts. *International Journal of Chemical Studies*, 2(5):27–34, 2015.
- [86] Kantam, M. L., Ranganath, K. V. S., Sateesh, M., Kumar, K. B. S., and Choudary, B. M. Friedel-Crafts acylation of aromatics and heteroaromatics by beta zeolite. *Journal of Molecular Catalysis A: Chemical*, 225(1):15–20, 2005.
- [87] Yamamoto, Y. and Itonaga, K. Versatile Friedel-Crafts-type alkylation of benzene derivatives using a molybdenum complex/ortho-chloranil catalytic system. *Chemistry—A European Journal*, 14(34):10705–10715, 2008.
- [88] Fan, C. M., Peng, Y., Zhu, Q., Lin, L., Wang, R. X., and Xu, A. W. Synproportionation reaction for the fabrication of Sn<sup>2+</sup> self-doped SnO<sub>2-x</sub> nanocrystals with tunable band structure and highly efficient visible light photocatalytic activity. *The Journal of Physical Chemistry C*, 117(46):24157–24166, 2013.
- [89] Choudhary, V. R. and Jana, S. K. Highly active and low moisture sensitive supported thallium oxide catalysts for Friedel-Crafts-type benzylation and acylation reactions: Strong thallium oxide–support interactions. *Journal of Catalysis*, 201(2):225–235, 2001.

- [90] Jana, S. K. Advances in liquid-phase Friedel-Crafts acylation of aromatics catalyzed by heterogeneous solids. *Catalysis Surveys from Asia*, 10(2):98–109, 2006.
- [91] Patil, M. L., Jnaneshwara, G. K., Sabde, D. P., Dongare, M. K., Sudalai, A., and Deshpande, V. H. Regiospecific acylations of aromatics and selective reductions of azobenzenes over hydrated zirconia. *Tetrahedron Letters*, 38(12):2137–2140, 1997.
- [92] Sarvari, M. H. and Sharghi, H. Reactions on a solid surface. A simple, economical and efficient Friedel-Crafts acylation reaction over zinc oxide (ZnO) as a new catalyst. *The Journal of Organic Chemistry*, 69(20):6953–6956, 2004.
- [93] Mu, M., Chen, L., Liu, Y., Fang, W., and Li, Y. An efficient Fe<sub>2</sub>O<sub>3</sub>/HY catalyst for Friedel-Crafts acylation of *m*-xylene with benzoyl chloride. *RSC Advances*, 4(70):36951–36958, 2014.
- [94] Rezaei, S. J. T., Nabid, M. R., Hosseini, S. Z., and Abedi, M. Polyaniline-supported zinc oxide (ZnO) nanoparticles: An active and stable heterogeneous catalyst for the Friedel-Crafts acylation reaction. *Synthetic Communications*, 42(10):1432–1444, 2012.
- [95] Reddy, K. R., Venkanna, D., Kantam, M. L., Bhargava, S. K. Srinivasu, P. SnO<sub>2</sub>–SiO<sub>2</sub> mesoporous composite: A very active catalyst for regioselective synthesis of aromatic ketones with unusual catalytic behavior. *Industrial & Engineering Chemistry Research*, 54(28):7005–7013, 2015.
- [96] Pasha, M. A., Manjula, K., and Jayashankara, V. P. Titanium dioxide-mediated Friedel-Crafts acylation of aromatic compounds in solvent-free condition under microwave irradiation. *Synthesis and Reactivity in Inorganic and Metal-Organic Chemistry*, 36(4):321–324, 2006.
- [97] Lanjekar, K. J. and Rathod, V. K. Microwave catalysis in organic synthesis. In Inamuddin, Boddula, R., and Asiri, A., M., editors, *Green Sustainable Process for Chemical and Environmental Engineering and Science*, pages 1–50. Elsevier, 2021.